Ore Geology Reviews 57 (2014) 518–538

Contents lists available at ScienceDirect

Ore Geology Reviews

journal homepage: www.elsevier.com/locate/oregeorev

Key factors controlling the accumulation of the Fe–Ti oxides in the Hongge layered intrusion in the Emeishan Large Igneous Province, SW China

Yan Luan [a,b], Xie-Yan Song [a,*], Lie-Meng Chen [a], Wen-Qin Zheng [a], Xiao-Qi Zhang [a,b], Song-Yue Yu [a], Yu-Wei She [a,b], Xiao-Lin Tian [c], Qi-Yu Ran [c]

[a] State Key Laboratory of Ore Deposit Geochemistry, Institute of Geochemistry, Chinese Academy of Sciences, Guiyang 550002, China
[b] University of Chinese Academy of Sciences, Beijing 100049, China
[c] 106 Geological Unit, Sichuan Bureau of Geology and Mineral Resources, Sichuan 617000, China

ARTICLE INFO

Article history:
Received 29 April 2013
Received in revised form 10 August 2013
Accepted 15 August 2013
Available online 7 September 2013

Keywords:
Hongge layered intrusion
Fractional crystallization
Parental magma
Magma replenishment
Footwall rock assimilation
Introduction of external H_2O

ABSTRACT

The Hongge layered intrusion hosts the largest Fe–Ti–V oxide ore deposit in the central part of the Emeishan Large Igneous Province, SW China. It is divided into Lower Zone (LZ), Middle Zone (MZ) and Upper Zone (UZ) from the bottom to the top. For the LZ, relatively higher Cr (250–3000 ppm) and Ni (50–200 ppm) contents of clinopyroxene, lower εNd_{259Ma} and higher $(^{87}Sr/^{86}Sr)_{259Ma}$ values (−2.82 to −0.07 and 0.7057–0.7076, respectively) and plenty of hornblende demonstrate a more primitive parental hydrous magma. In contrast, relatively low Cr (<150 ppm) and Ni (<100 ppm) of the clinopyroxene, high εNd_{259Ma} and low $(^{87}Sr/^{86}Sr)_{259Ma}$ values (−0.32 to 0.49 and 0.7058 to 0.7063, respectively) suggest that the MZ rocks were formed from more evolved, Fe–Ti enriched, and weakly contaminated magmas. MELTS calculation indicates that H_2O played a key role in the early crystallization of magnetite and occurrence of abundance of hornblende in the LZ. Whereas, the critical factor for the formation of the massive Fe–Ti oxide layers at the bases of the cyclic units in the MZ is coupling of early crystallization of Fe–Ti oxides from the Fe–Ti highly enriched magma and gravitational resorting and settling of the Fe–Ti oxides. Such magmas were produced by fractional crystallization of olivine and pyroxene in deep-seated magma chamber, and compositional reversals of the cyclic units show repeatedly replenishment of such magmas from deep level. Extensively fractionation during the formation of the LZ and MZ resulted in phosphorus saturation and the formation of the apatite magnetite gabbros in the UZ.

1. Introduction

Fe–Ti oxides commonly crystallize late during fractionation of basaltic magma and cumulate in the upper parts of layered intrusions in the world, such as in the Bushveld Igneous Complex (Eales and Cawthorn, 1996; Lee, 1996; Scoon and Mitchell, 1994), the Skaergaard intrusion (McBirney, 1996), and the Muskox intrusion (Irvine, 1977). However, thick V–Ti-magnetite ore layers occur in the lower half of the layered intrusions in the central part of the Emeishan Large Igneous Province (ELIP), SW China (Pang et al., 2008; Panxi Geological Unit, 1984; Song et al., 2013). Recent studies have indicated that these layered intrusions represent the intrusive facies of the Permian Emeishan flood basalts which resulted from a ~260 Ma mantle plume (Song et al., 2001; Xu et al., 2001; Zhou et al., 2002) (Fig. 1). Some of the layered intrusions contact with Neoproterozoic limestones at their footwall. Thus, it has been suggested that the reaction between the mafic magma and the footwall limestone resulted in elevation of oxygen fugacity, early crystallization of Fe–Ti oxide and the formation of the Fe–Ti oxide ore layers in the Lower Zone of the Panzhihua intrusion (Ganino et al., 2008).

However, for the Hongge intrusion, the dominant Fe–Ti oxide ore layers occur in the Middle Zone, instead of in the Lower Zone (Figs. 2b and 3). Bai et al. (2012) demonstrated the extensive accumulation of Fe–Ti oxides and the formation of the massive ore layers in the Middle Zone by the model of early crystallization of the Fe–Ti oxides resulted from oxygen fugacity elevation due to assimilation of the footwall limestone. However, we note that the sample used in study of Bai et al. (2012) was collected from the open pit, which only focused on mining of the Middle Zone Fe–Ti oxide ore layers, why the Fe–Ti oxides accumulated weakly in the Lower Zone and Upper Zone has not been addressed yet in fact. In summary, the following questions need to be addressed: (1) What is the compositional difference of the parental magmas of the three zones? (2) Whether or not did assimilation of wallrock or introduction of H_2O result in early crystallization of Fe–Ti oxides in the LZ? (3) What is the critical factor leading to extensive accumulation of Fe–Ti oxides in the MZ?

* Corresponding author at: State Key Laboratory of Ore Deposit Geochemistry Institute of Geochemistry, Chinese Academy of Sciences 46th Guanshui Road, Guiyang 550002, China. Tel.: +86 851 5895538; fax: +86 851 5891664.
E-mail address: songxieyan@vip.gyig.ac.cn (X.-Y. Song).

0169-1368/$ – see front matter © 2013 Elsevier B.V. All rights reserved.
http://dx.doi.org/10.1016/j.oregeorev.2013.08.010

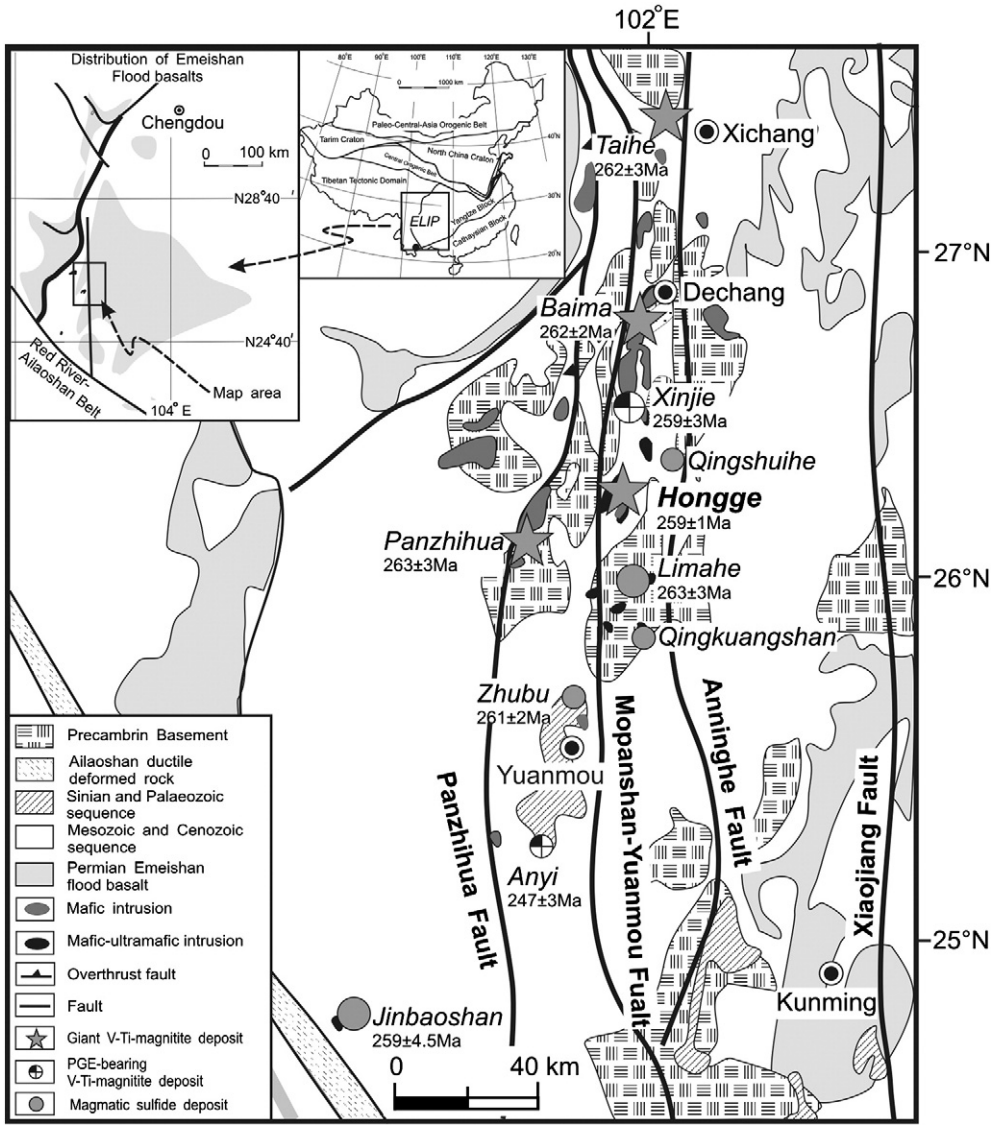

Fig. 1. Simplified regional geological map of the Central ELIP, showing the distribution of layered intrusions hosting giant Fe–Ti oxide deposits. Ages of these intrusions are from Zhou et al. (2002, 2005, 2008), Guo et al. (2004), Zhong and Zhu (2006), Tao et al. (2009) and Yu et al. (2014).
Modified after Song et al. (2009).

In this study, the three lithologic zones of the Hongge intrusion have been sampled from bore holes. Detailed petrographic investigation, geochemical studies of whole-rocks and minerals as well as MELTS calculations lead us to maintain that the parental magmas of the three zones experienced different degrees of fractional crystallization in the deep-seated magma chamber and crustal contamination in the shallow magma chamber. The most critical factors for the formation of the massive Fe–Ti oxide ore layers are (1) the early crystallization of the Fe–Ti oxides from Fe–Ti enriched magma from deep level due to fractional crystallization of mafic minerals and (2) accumulation of amount of the Fe–Ti oxides.

2. Geological background

The ELIP comprises of the Middle/Late Permian continental flood basalts, genetically related contemporary mafic–ultramafic intrusions and felsic intrusions resulted from a mantle plume (zircon U–Pb dated at ~260 Ma), and covers an area more than 5×10^5 km^2 in southwestern China and northern Vietnam (Fig. 1) (Chung and Jahn, 1995; Song et al., 2001; Xu et al., 2001; Zhou et al., 2002). It can be divided into a central part and an outer zone (Song et al., 2009). The central part of the ELIP is characterized by low-Ti basalts (Ti/Y < 500) overlain by high-Ti basalts (Ti/Y > 500) (Song et al., 2004; Xiao et al., 2004; Xu et al., 2001) and occurrences of large layered intrusions hosting giant V–Ti-magnetite deposits and numerous syenite and granite plutons. Whereas, the outer zone of the ELIP predominantly consists of high-Ti basalts.

In the central ELIP, the most important layered mafic–ultramafic intrusions hosting giant V–Ti-magnetite deposits distribute along a series of N–S trending faults, and include from north to south: Taihe (262 ± 3 Ma, Guo et al., 2004), Baima (262 ± 3 Ma, Zhou et al., 2008), Xinjie (259 ± 3 Ma, Zhou et al., 2002), Hongge (259 ± 1.3 Ma, Zhong and Zhu, 2006) and Panzhihua (263 ± 3 Ma, Zhou et al., 2005) (Fig. 1). They are mafic intrusions consisting of gabbros (such as Taihe, Baima, and Panzhihua) or mafic–ultramafic intrusions comprising of gabbros and clinopyroxenites (such as Hongge and Xinjie) (Panxi Geological Unit, 1984). Some small mafic–ultramafic intrusions contain magmatic sulfide mineralization in both the central ELIP (such as Limahe and Qingkuangshan) and outer zone of the ELIP (such as Yangliuping and

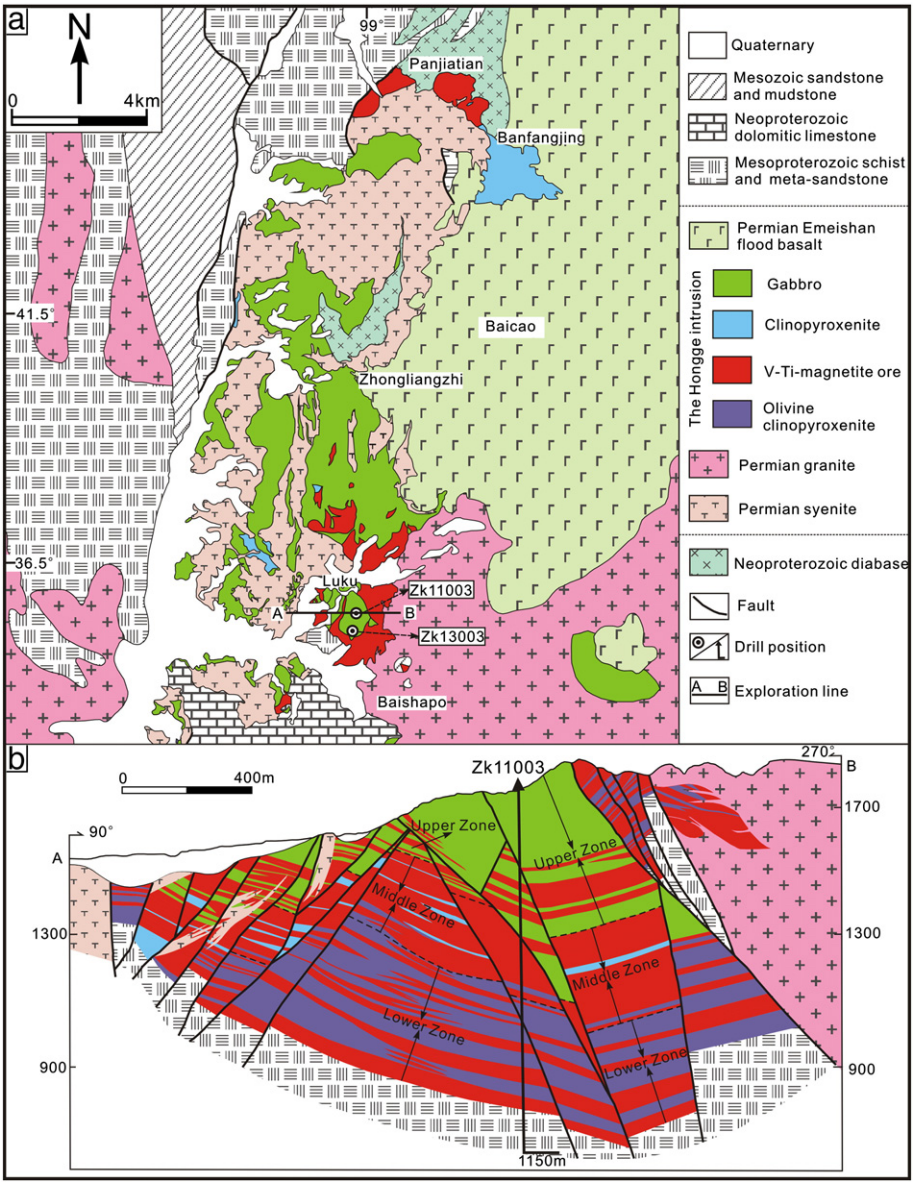

Fig. 2. a: Geological map of the Hongge layered intrusion; b: cross section of the exploration line. Modified after Sichuan Geological Survey (2010).

Baimazhai) (Song et al., 2008b). It has been proposed that the Fe–Ti oxide deposits and magmatic Cu–Ni–(PGE) sulfide deposits in the central ELIP are genetically related to the high-Ti and low-Ti basaltic magmas, respectively (Fig. 1) (Song et al., 2005; Zhou et al., 2008).

3. Petrography of the Hongge layered intrusion

The flat Hongge intrusion is ~16 km long, ~5–10 km wide and ~1.2 km thick (Fig. 2a). The outcropping rocks of the Hongge intrusion are mainly the Upper Zone gabbros and the Middle Zone clinopyroxenites and V–Ti-magnetite ore layers (Fig. 2a). This intrusion is emplaced in Mesoproterozoic schists and meta-sandstones in the north, in Neoproterozoic dolomitic limestones in the south, and in Permian Emeishan flood basalts at the northeast corner of the intrusion (Bai et al., 2012; Panxi Geological Unit, 1984) (Fig. 2a). The contact relationship is only preserved locally because of the emplacement of slightly later Permian granite and syenite around the Hongge intrusion (255.2 ± 3.6 Ma) (Xu et al., 2008) (Fig. 2a, b).

Based on mineral assemblages and lithologic textures, the Hongge layered intrusion can be divided into Lower Zone (LZ), Middle Zone (MZ) and Upper Zone (UZ) (Fig. 3). The LZ is characterized by containing as high as 5–15 modal% hornblendes and biotite, the MZ is defined by the occurrence of massive Fe–Ti oxide ore layers, and the UZ is marked by the appearance of abundant euhedral apatite.

3.1. Lower Zone (LZ)

The LZ rocks are characterized by plenty of hornblende and biotite and comprise of hornblende (magnetite) clinopyroxenite and hornblende (magnetite) olivine clinopyroxenite. The hornblende clinopyroxenite contains 70–75 modal% clinopyroxene, 8–20% Fe–Ti oxides, 7–10% hornblende, locally up to 8% biotite, less than 5% olivine and minor plagioclase and apatite. The hornblende olivine clinopyroxenites contain more olivine (10–35%) and less clinopyroxene (40–75%) relative to the hornblende clinopyroxenite. When the Fe–Ti oxides increase to more than 20%, it is named as hornblende magnetite clinopyroxenite or hornblende magnetite olivine clinopyroxenite (Figs. 3, 4a). The LZ

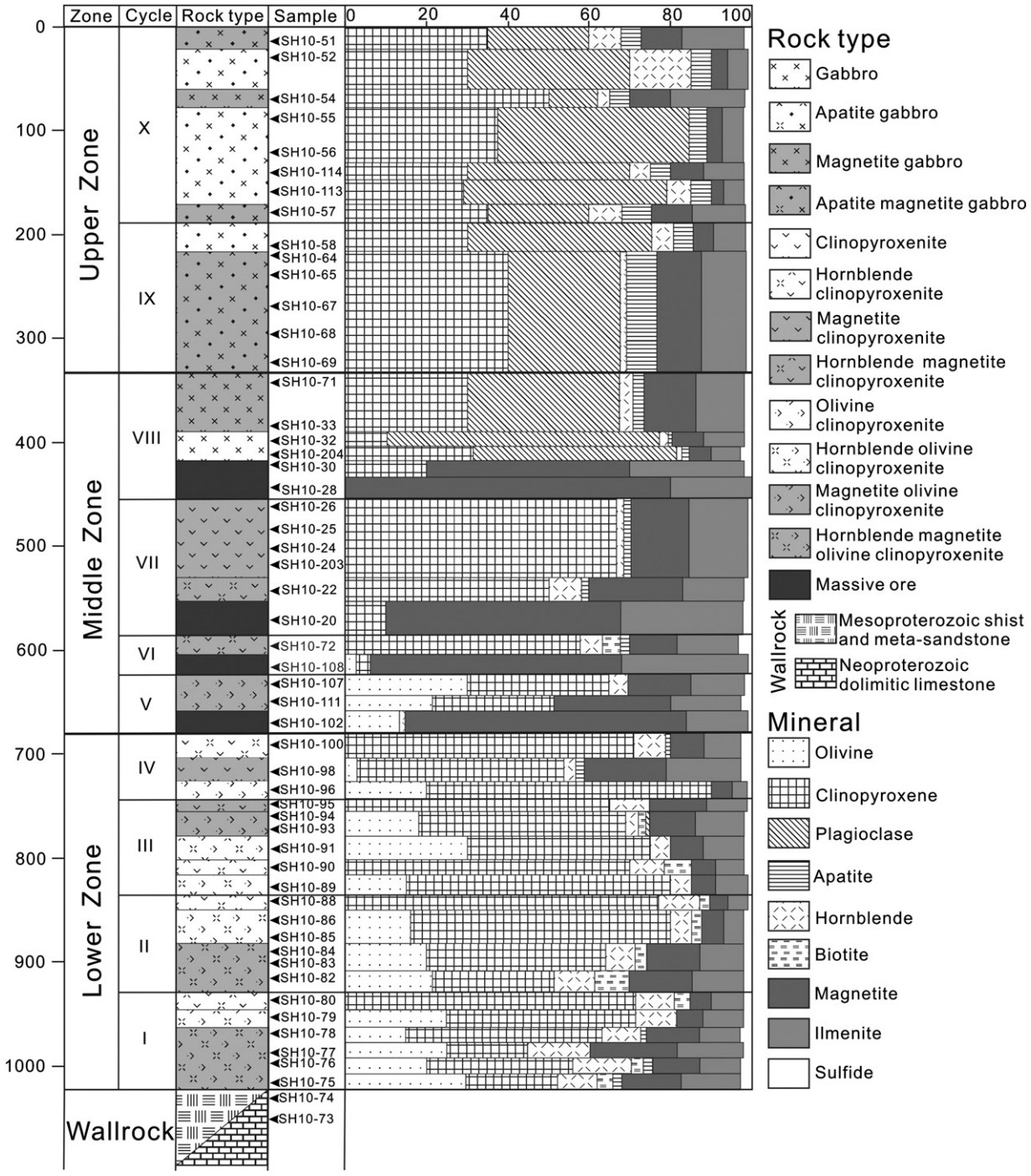

Fig. 3. Stratigraphic column of the Hongge layered intrusion, showing lithologic subdivision, mineral proportions and location of the samples.

can be further subdivided into four cycles (I to IV from the base to the top) (Fig. 3). In each cycle unit, the hornblende (magnetite) olivine clinopyroxenite is overlain by the hornblende (magnetite) clinopyroxenite as contents of olivine decrease upwards.

As shown in Fig. 4a, magnetite in the LZ rocks occurs as euhedral grains and is enclosed in large clinopyroxene crystals, indicating that the magnetite crystallized earlier than clinopyroxene. Two sets of exsolution magnetite lamellaes oriented parallel to the prismatic cleavage occur in the clinopyroxene grains (Fig. 4b). It is noteworthy that the Hongge LZ rocks contain much more hornblende than the rocks of the Panzhihua and Baima intrusions, in which the interstitial hornblende is less than 2 modal% (Panxi Geological Unit, 1984; Song et al., 2013; Zhang et al., 2012). Olivine (0.5–5 mm) and clinopyroxene (0.1–5 mm) are poikilitically enclosed by hornblende (Fig. 4a). Poikilitic texture and homogeneous interference color indicate that the hornblende is primary magmatic origin, rather than the production of hydrothermal alteration (Fig. 4a). Biotite, apatite and plagioclase are always interstitial (Fig. 4c). The textural features suggest that olivine and Fe–Ti oxides crystallized earlier than clinopyroxene, which was earlier than hornblende, biotite, plagioclase and apatite.

3.2. Middle Zone (MZ)

The MZ comprises of massive Fe–Ti oxide ore, magnetite olivine clinopyroxenite, magnetite clinopyroxenite, magnetite gabbro and

gabbro. Comparing with the LZ rocks, the MZ rocks contain less hornblende (Fig. 3). The massive ore consists of more than 85 modal% Fe–Ti oxides and less than 15% olivine or clinopyroxene. The magnetite olivine clinopyroxenite contains 20–50% Fe–Ti oxides, 20–30% olivine and 30–35% clinopyroxene. When olivine decreases to less than 5% and clinopyroxene increases to 60–75%, it is named as magnetite clinopyroxenite. The magnetite gabbro consists of 20–28% Fe–Ti oxides, 30–45% clinopyroxene and 25–37% plagioclase, when the Fe–Ti oxides are less than 20%, it is named as gabbro. Hornblende in the MZ rocks is interstitial, generally lower than 3% and locally up to 5–8%. In this study, we

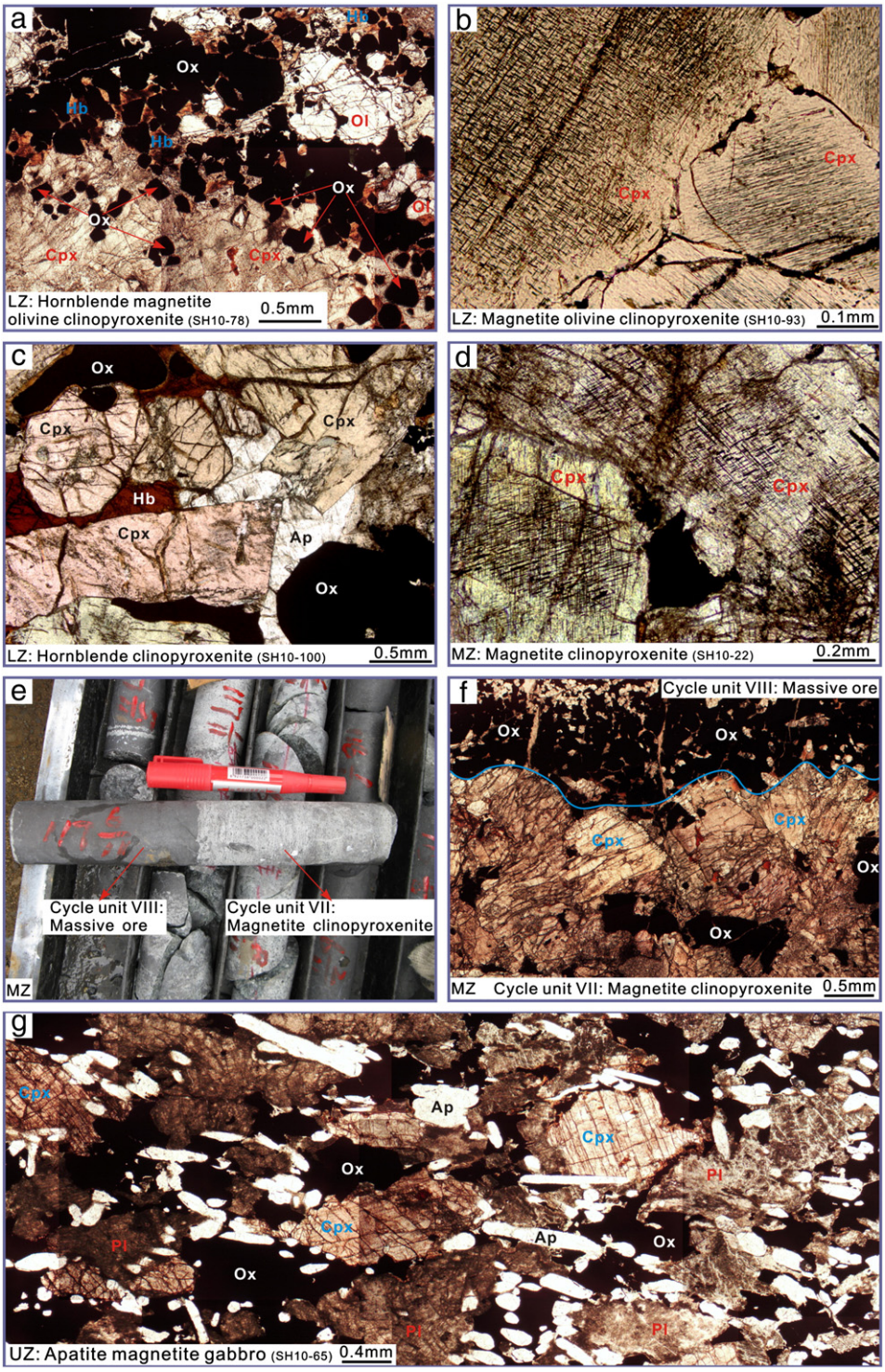

Fig. 4. Microscope photos of the rocks of the Hongge intrusion under plane-polarized light. a: Euhedral magnetite enclosed in clinopyroxene crystal and interstitial hornblende in the LZ hornblende magnetite olivine clinopyroxenite; b: orientated exclusion magnetite lamella in the clinopyroxene crystal in the LZ magnetite clinopyroxenite; c: interstitial apatite and hornblende between oxides and clinopyroxene in the hornblende clinopyroxenite; d: orientated exclusion magnetite lamella in the clinopyroxene crystal in the MZ magnetite clinopyroxenite; e and f: sharp contact between the cycle unit VIII massive ore and the underlying cycle unit VII magnetite clinopyroxenite in hand sample and under microscope, respectively; g: orientated apatite in the UZ apatite magnetite gabbro. Ol = Olivine; Cpx = Clinopyroxene; Pl = Plagioclase; Hb = Hornblende; Ap = Apatite; Ox = Fe–Ti oxide.

Table 1
Major and trace element compositions of the rocks of the Hongge intrusion.

Zone			Lower Zone					
Cycle			I					
Sample	SH10-73	SH10-74	SH10-75	SH10-76	SH10-77	SH10-78	SH10-79	SH10-80
Rock type	Wallrock	Wallrock	Mt-Ocp	Mt-Ocp	Mt-Ocp	Mt-Ocp	Ocp	Cpx
Depth/m	1047	1028	1017	998	988	968	954	937
Major oxides (wt.%)								
SiO_2	58.2	57.2	25.1	34.6	24.1	33.7	39.9	40.6
TiO_2	1.01	0.73	10.95	6.24	9.66	6.06	3.93	4.34
Al_2O_3	19.3	20.3	5.70	4.40	4.51	4.36	4.20	7.34
Fe_2O_3	5.00	5.96	19.8	11.8	19.2	14.4	6.59	7.04
FeO	–	–	19.5	12.6	20.5	12.5	11.8	11.8
MnO	0.07	0.07	0.25	0.22	0.24	0.22	0.19	0.20
MgO	3.05	2.89	7.60	15.4	10.9	15.1	16.6	13.2
CaO	0.87	0.70	7.34	10.9	7.85	10.6	14.6	12.2
Na_2O	0.31	1.85	0.50	0.51	0.44	0.50	0.50	1.00
K_2O	8.71	7.79	0.66	0.36	0.18	0.26	0.08	0.65
P_2O_5	0.40	0.20	0.09	0.19	0.11	0.11	0.08	0.24
SO_3	–	–	0.51	1.44	0.82	0.75	0.66	0.11
LOI	2.50	2.11	–	–	–	–	0.33	–
Total	99.5	99.8	98.0	98.6	98.5	98.4	99.4	98.6
$(Fe_2O_3)_T$	5.0	6.0	41.5	25.8	42.0	28.3	19.7	20.1
Fe^{3+}/Fe^{2+}	0.92	0.92	0.92	0.84	0.85	1.04	0.50	0.54
Fe^{3+}/Ti^{4+}	1.81	1.81	1.81	1.89	1.99	2.38	1.68	1.62
Trace elements (ppm)								
Sc	15.1	23.5	21.7	30.3	24.6	30.3	44.1	39.3
V	108	105	1240	653	1500	679	578	535
Cr	85.8	83	2530	963	2430	2470	1250	1250
Co	18.7	14	162	135	186	129	131	95
Ni	38.0	24	621	615	747	648	416	415
Cu	113	14	105	276	339	250	215	237
Rb	221	180	42.9	23.1	7.5	16.4	2.84	32.5
Sr	206	164	107	218	165	148	177	180
Y	19.9	22.3	11.3	10.7	6.6	8.6	10.6	18.6
Zr	225	111	56.7	75.7	50.0	49.5	50.0	127.0
Nb	17.5	8.20	15.9	13.5	8.71	6.82	5.17	13.0
Ba	737	712	52.0	84.4	59.4	57.5	44.9	160
La	49.0	43.8	10.2	8.58	6.51	5.44	5.88	17.10
Ce	91.8	84.7	23.8	22.5	15.5	15.6	16.3	39.5
Pr	8.77	8.88	3.07	3.37	2.21	2.44	2.64	5.45
Nd	25.3	30.1	12.8	15.7	10.7	12.2	13.7	23.6
Sm	3.91	5.18	2.94	3.63	2.50	3.08	3.84	5.70
Eu	1.40	1.30	0.74	1.13	0.78	0.95	1.19	1.68
Gd	3.93	5.35	2.70	3.41	2.28	2.70	3.43	5.13
Tb	0.57	0.75	0.43	0.49	0.32	0.39	0.51	0.77
Dy	3.05	3.78	2.27	2.31	1.60	1.95	2.58	4.12
Ho	0.71	0.84	0.45	0.43	0.26	0.38	0.43	0.84
Er	2.13	2.43	1.14	1.00	0.70	0.83	1.08	1.97
Tm	0.30	0.35	0.15	0.13	0.09	0.11	0.14	0.25
Yb	2.32	2.37	0.94	0.73	0.47	0.58	0.77	1.51
Lu	0.40	0.36	0.14	0.12	0.06	0.10	0.10	0.23
Hf	5.60	3.02	2.12	3.24	1.67	2.05	1.96	4.23
Ta	1.17	0.47	1.29	1.12	0.63	0.58	0.38	0.99
Th	16.9	14.3	3.13	1.23	0.83	0.83	0.46	2.01
U	2.30	2.08	1.67	0.31	0.22	0.22	0.10	0.41
Pb	14.6	12.4	4.3	11.4	8.3	31.1	14.0	13.4

Lower Zone								
II						III		
SH10-82	SH10-83	SH10-84	SH10-85	SH10-86	SH10-88	SH10-89	SH10-90	SH10-91
Mt-Ocp	Mt-Ocp	Mt-Ocp	Ocp	Ocp	Cpx	Ocp	Cpx	Ocp
916	902	891	877	860	842	828	810	792
Major oxides (wt.%)								
28.2	36.6	37.9	40.7	41.7	40.0	43.4	39.7	37.6
7.17	5.34	3.33	3.01	3.20	5.38	1.59	4.87	5.52
4.67	6.36	3.79	4.02	4.65	5.85	7.07	4.61	2.60
16.2	11.0	9.1	7.7	7.6	5.7	4.1	9.1	6.0
17.3	12.2	11.4	8.9	7.5	10.0	8.3	9.5	13.3
0.24	0.21	0.21	0.16	0.19	0.22	0.19	0.18	0.22
12.9	13.8	20.0	17.1	16.1	17.1	16.8	14.6	20.5
8.11	10.7	10.1	14.4	16.1	12.3	13.0	14.5	11.0

(continued on next page)

Table 1 (*continued*)

Lower Zone								
II						III		
SH10-82	SH10-83	SH10-84	SH10-85	SH10-86	SH10-88	SH10-89	SH10-90	SH10-91
Mt-Ocp	Mt-Ocp	Mt-Ocp	Ocp	Ocp	Cpx	Ocp	Cpx	Ocp
916	902	891	877	860	842	828	810	792
Major oxides (wt.%)								
0.40	0.71	0.49	0.51	0.38	0.49	0.48	0.51	0.33
0.36	1.02	0.30	0.13	0.02	0.07	0.49	0.62	0.05
0.08	0.14	0.07	0.04	0.05	0.04	0.02	0.06	0.05
0.78	0.53	0.72	1.34	0.09	–	–	0.64	–
1.63	–	0.66	1.88	1.00	1.19	3.14	–	0.85
98.0	98.6	98.0	99.8	98.5	98.2	98.4	98.9	98.0
35.4	24.6	21.7	17.5	15.9	16.8	13.3	19.7	20.7
0.85	0.82	0.72	0.78	0.92	0.51	0.44	0.86	0.41
2.26	2.07	2.73	2.55	2.38	1.06	2.55	1.87	1.09
Trace elements (ppm)								
26.1	33.2	27.9	44.5	50.7	42.4	42.8	45.7	31.6
1230	670	410	485	405	356	333	563	446
2410	1560	1100	1190	1470	1330	1510	1120	1350
167	120	131	128	87	88	98	99	133
656	516	630	596	225	439	222	360	766
260	162	309	354	30	18	13	152	96
22.7	54.8	13.6	4.72	1.49	2.37	47.6	56.8	2.33
124	250	107	65.7	85.9	183	215	87.1	88.6
7.5	11.3	9.2	10.3	12.0	13.6	10.5	11.2	8.0
55.7	72.0	45.0	41.0	46.4	51.2	31.1	43.1	38.2
7.70	9.13	4.79	2.82	3.27	15.10	1.12	4.30	6.46
51.0	117	30.8	13.4	8.04	15.5	40.5	34.5	7.37
8.71	10.5	5.93	3.81	4.17	3.18	2.54	3.99	2.75
17.1	25.8	15.7	12.7	14.3	12.0	8.80	13.2	9.19
2.24	3.47	2.31	2.27	2.52	2.43	1.67	2.25	1.68
10.0	15.5	11.5	12.7	13.7	13.9	9.57	12.6	9.32
2.39	3.78	3.00	3.70	3.98	4.52	2.94	3.55	2.65
0.77	1.14	0.99	1.03	1.33	1.29	1.08	1.08	0.96
2.18	3.44	2.70	3.49	3.84	4.24	2.86	3.79	2.68
0.33	0.47	0.39	0.51	0.54	0.61	0.46	0.53	0.38
1.62	2.36	2.01	2.43	2.75	3.31	2.47	2.63	1.99
0.30	0.47	0.40	0.43	0.55	0.62	0.44	0.52	0.36
0.75	1.15	1.00	1.07	1.26	1.44	1.12	1.19	0.87
0.10	0.14	0.12	0.13	0.16	0.17	0.13	0.14	0.09
0.61	0.84	0.69	0.75	0.91	1.15	0.88	0.83	0.57
0.08	0.12	0.11	0.10	0.14	0.17	0.12	0.13	0.08
1.82	2.57	1.96	1.90	2.05	2.45	1.29	2.05	1.69
0.52	0.78	0.43	0.22	0.31	1.47	0.11	0.43	0.54
2.13	2.21	1.26	0.41	0.23	0.08	0.04	0.35	0.12
0.23	0.48	0.27	0.10	0.05	0.01	0.01	0.13	0.03
26.6	24.8	13.6	10.4	7.1	13.7	9.84	15.6	10.5

Lower Zone						Middle Zone		
III			IV			V		
SH10-93	SH10-94	SH10-95	SH10-96	SH10-98	SH10-100	SH10-102	SH10-111	SH10-107
Mt-Ocp	Mt-Ocp	Mt-Cpx	Ocp	Mt-Cpx	Cpx	Mass-Ore	Mt-Ocp	Mt-Ocp
773	760	749	735	717	692	671	651	633
Major oxides (wt.%)								
35.6	33.0	27.1	40.5	22.2	41.6	4.9	19.2	26.4
6.86	7.07	18.50	3.08	15.40	4.22	14.10	7.69	5.09
4.21	4.34	3.69	3.68	3.72	4.49	3.33	2.14	2.26
13.4	13.5	6.8	8.5	18.3	5.3	35.9	23.4	16.9
10.2	14.0	18.5	7.1	17.5	8.4	23.3	16.1	12.9
0.20	0.20	0.38	0.16	0.24	0.16	0.27	0.23	0.16
12.9	11.5	10.5	16.7	9.7	12.6	10.3	19.9	23.9
15.5	14.2	10.7	15.2	9.9	19.1	0.1	0.6	2.9
0.33	0.38	0.39	0.32	0.24	0.35	0.10	0.14	0.23
–	0.14	1.25	0.42	–	0.14	–	0.03	0.04
0.01	0.02	0.10	0.01	0.02	0.22	–	0.02	0.09
0.09	–	0.21	0.38	1.54	0.61	1.60	2.16	1.18
–	0.07	–	2.52	–	1.39	1.38	4.81	5.44
99.2	98.4	98.2	98.6	98.7	98.5	95.2	96.4	97.4
24.7	29.1	27.4	16.4	37.7	14.6	61.8	41.3	31.2
1.19	0.87	0.33	1.08	0.95	0.57	1.39	1.31	1.18
1.96	1.91	0.37	2.78	1.19	1.26	2.55	3.04	3.31

Table 1 (*continued*)

Lower Zone						Middle Zone		
III			IV			V		
SH10-93	SH10-94	SH10-95	SH10-96	SH10-98	SH10-100	SH10-102	SH10-111	SH10-107
Mt-Ocp	Mt-Ocp	Mt-Cpx	Ocp	Mt-Cpx	Cpx	Mass-Ore	Mt-Ocp	Mt-Ocp
773	760	749	735	717	692	671	651	633
Trace elements (ppm)								
50.3	41.4	42.0	42.9	36.2	54.5	11.4	7.39	11.6
757	1110	705	385	1120	430	1840	960	600
672	1320	372	1460	159	65	5480	4730	2670
103	139	119	88	159	88	265	203	185
315	337	278	388	237	133	1060	1420	791
90	61	101	65	163	120	464	1042	84
0.59	7.31	87.9	34.1	0.74	8.08	0.1	7.5	2.0
93.1	93.6	96.8	135	69.8	459	3.22	9.16	53.7
10.0	10.1	9.30	10.1	6.61	18.4	0.2	5.0	2.8
39.6	42.7	99.4	31.3	53.3	61.0	12.5	17.1	20.7
3.44	3.46	30.20	0.76	11.70	6.99	2.50	9.54	3.83
3.59	13.6	79.3	15	5.47	40	1.94	14.1	25
2.44	3.57	4.86	2.26	2.07	10.9	0.10	5.72	3.38
9.77	11.7	13.8	9.10	7.24	29.3	0.23	8.01	7.96
1.86	2.05	2.26	1.82	1.32	4.42	0.03	0.72	1.07
10.8	11.6	11.9	10.6	7.31	21.5	0.18	2.29	5.08
3.65	3.41	3.16	3.48	2.32	5.73	0.06	0.53	1.26
1.09	1.09	1.02	1.07	0.80	1.63	0.01	0.15	0.35
3.41	3.40	2.96	3.28	2.17	5.29	0.03	0.48	1.09
0.48	0.46	0.44	0.46	0.32	0.79	0.01	0.08	0.15
2.48	2.36	2.17	2.40	1.57	4.05	0.03	0.53	0.65
0.46	0.41	0.44	0.51	0.29	0.85	0.01	0.12	0.13
0.98	1.07	0.99	1.10	0.67	2.01	0.03	0.35	0.34
0.13	0.12	0.11	0.13	0.08	0.26	0.00	0.06	0.04
0.73	0.74	0.76	0.71	0.49	1.59	0.02	0.38	0.23
0.11	0.10	0.11	0.11	0.08	0.25	0.00	0.07	0.04
2.15	1.69	3.91	1.85	2.49	2.88	0.58	0.68	0.87
0.42	0.26	3.25	0.12	1.48	0.59	0.34	0.34	0.38
0.07	0.42	0.44	0.05	0.12	1.60	0.02	0.39	0.43
0.01	0.11	0.11	0.13	0.02	0.33	0.00	0.03	0.09
9.77	6.83	11.6	7.42	6.47	9.29	2.44	2.86	2.23

Middle Zone								
VI		VII						VIII
SH10-108	SH10-72	SH10-20	SH10-22	SH10-203	SH10-24	SH10-25	SH10-26	SH10-28
Mass-Ore	Mt-Cpx	Mass-Ore	Mt-Cpx	Mt-Cpx	Mt-Cpx	Mt-Cpx	Mt-Cpx	Mass-Ore
617	596	571	543	518.5	503	484	462	443.5
Major oxides (wt.%)								
1.9	30.1	7.6	28.7	32.6	29.1	31.1	27.5	1.0
18.81	10.70	15.25	8.43	7.81	13.80	11.05	14.88	17.40
3.79	4.44	3.55	4.30	4.45	3.90	3.41	4.46	3.09
38.4	12.8	34.7	14.8	13.4	9.7	11.4	7.4	34.9
27.1	14.7	25.6	16.2	13.9	15.8	14.1	19.3	30.9
0.33	0.22	0.23	0.23	0.19	0.19	0.19	0.36	0.30
7.2	10.7	7.6	10.1	10.6	10.3	10.8	10.2	6.8
0.2	13.4	1.6	12.4	14.6	13.3	15.5	11.7	0.2
0.16	0.36	0.05	0.50	0.25	0.21	0.13	0.26	0.05
0.02	0.15	–	0.78	0.01	0.01	–	0.51	–
0.03	0.04	–	0.06	0.06	0.05	0.05	0.59	–
–	1.16	0.29	0.77	0.17	0.66	1.14	–	4.33
–	–	0.06	1.48	0.65	0.72	1.25	0.79	1.43
98.0	98.6	96.5	98.7	98.6	97.6	100.0	97.9	100.3
68.5	29.1	63.1	32.7	28.8	27.2	27.0	28.9	69.2
1.28	0.78	1.22	0.82	0.87	0.56	0.73	0.35	1.02
2.04	1.19	2.27	1.75	1.71	0.70	1.03	0.50	2.00
Trace elements (ppm)								
11.0	36.2	10.6	36.7	42.0	42.4	43.4	45.7	10.4
2730	796	2450	1230	1090	914	910	881	2520
1540	131	5510	179	256	57	76	47	4570
278	125	283	140	118	132	121	114	224
681	347	1076	401	304	267	239	169	650
141	305	223	266	210	240	219	186	242
0.1	14.0	0.2	68.4	2.3	2.4	0.4	24.1	0.3
3.35	117	4.57	157	96.3	81.7	86.7	91.8	7.42
0.5	11.1	0.3	9.4	8.9	8.2	9.5	30.7	0.3

(*continued on next page*)

Table 1 (*continued*)

Middle Zone								
VI		VII						VIII
SH10-108	SH10-72	SH10-20	SH10-22	SH10-203	SH10-24	SH10-25	SH10-26	SH10-28
Mass-Ore	Mt-Cpx	Mass-Ore	Mt-Cpx	Mt-Cpx	Mt-Cpx	Mt-Cpx	Mt-Cpx	Mass-Ore
617	596	571	543	518.5	503	484	462	443.5
20.7	61.1	15.4	40.6	39.4	59.7	50.7	134	14.9
5.21	10.0	3.09	7.43	4.74	13.6	9.23	62.6	3.18
1.48	12.5	7.68	42.4	16.3	15.5	9.85	384	5.92
0.63	6.87	0.36	5.80	3.74	3.27	3.46	30.00	0.20
1.39	15.2	0.85	14.5	11.6	10.3	11.0	71.1	0.52
0.18	2.29	0.12	2.24	2.03	1.76	1.99	9.60	0.08
0.84	11.3	0.67	11.4	11.1	10.1	11.2	42.8	0.47
0.18	3.06	0.08	3.12	3.15	2.90	3.34	9.64	0.10
0.04	0.98	0.04	0.96	1.03	0.92	1.03	2.45	0.02
0.12	3.18	0.08	2.93	3.06	2.80	3.14	8.69	0.08
0.02	0.38	0.01	0.45	0.44	0.40	0.45	1.29	0.01
0.11	2.00	0.05	2.24	2.25	2.00	2.29	6.42	0.06
0.02	0.38	0.01	0.38	0.36	0.33	0.39	1.16	0.01
0.06	0.91	0.03	0.98	0.88	0.82	0.98	3.10	0.03
0.01	0.11	0.00	0.11	0.10	0.10	0.11	0.39	0.00
0.04	0.64	0.03	0.68	0.60	0.57	0.62	2.49	0.03
0.01	0.09	0.00	0.09	0.09	0.08	0.09	0.34	0.00
0.82	2.00	0.61	1.83	1.86	2.25	2.03	3.76	0.63
0.49	0.86	0.32	0.48	0.40	1.21	0.83	3.05	0.34
0.07	1.97	0.03	0.90	0.21	0.16	0.17	0.84	0.02
0.02	0.15	0.01	0.21	0.05	0.04	0.04	0.28	0.00
0.38	7.52	2.91	7.63	2.85	1.69	2.01	1.51	1.37

Middle Zone					Upper Zone			
VIII					IX			
SH10-30	SH10-204	SH10-32	SH10-33	SH10-71	SH10-69	SH10-68	SH10-67	SH10-65
Mass-Ore	Gb	Gb	Mt-Gb	Mt-Gb	Mt-Gb	Mt-Gb	Mt-Gb	Mt-Gb
422	413	399	384.5	343	323	297	270	239
Major oxides (wt.%)								
8.8	37.2	34.0	33.8	26.7	32.2	28.7	28.2	18.5
20.31	8.34	6.84	8.10	9.01	7.81	8.18	8.50	12.0
4.47	17.17	19.09	5.16	16.0	11.0	9.34	10.4	10.4
25.2	0.9	6.8	8.5	8.9	7.8	8.6	10.0	11.5
28.6	12.3	10.9	14.8	15.0	13.0	12.0	11.9	15.9
0.32	0.12	0.11	0.19	0.18	0.19	0.20	0.20	0.19
6.8	4.0	3.5	10.8	3.8	5.2	6.6	6.2	4.3
2.1	11.4	11.0	14.8	13.2	12.8	17.1	15.4	15.8
0.14	1.11	0.35	0.24	0.13	1.70	0.47	0.74	0.13
0.02	2.32	2.76	0.05	0.01	0.44	–	0.36	–
0.05	0.21	0.10	0.06	0.40	3.27	3.59	3.69	5.77
–	–	–	–	1.10	1.25	1.16	0.98	1.24
0.17	2.49	3.09	1.31	3.12	1.34	1.98	1.41	1.68
96.9	97.4	98.5	97.8	97.4	97.9	97.9	98.0	97.3
57.0	14.5	18.8	24.9	25.5	22.2	21.9	23.2	29.2
0.80	0.06	0.56	0.52	0.54	0.54	0.65	0.76	0.65
1.24	0.10	0.99	1.06	0.99	0.99	1.05	1.18	0.96
Trace elements (ppm)								
17.6	12.1	8.82	42.9	9.15	13.4	16.3	15.6	9.6
1990	492	647	950	641	529	518	563	723
112	37	227	169	14	10.6	10.6	68.3	16.7
207	50	73	106	81	66.6	65.7	63.2	95.4
133	25	64	158	17	6.23	4.78	10.6	6.66
152	57	59	128	58	36.9	33.9	33.3	41.2
0.8	93.7	137.0	8.0	1.7	21.6	0.95	21.1	1.6
18.7	1670	1880	370	2490	1160	1460	1660	1720
3.9	6.7	4.0	12.1	6.7	27.8	26.5	26.9	30.9
46.9	51.9	26.5	53.2	39.7	137.0	40.1	38.3	34.8
13.8	13.0	6.49	6.78	12.6	20.5	10.6	9.67	12.8
7.53	334	195	8.6	9.43	148	6.01	101	11.2
2.09	8.29	5.04	4.53	6.92	37.60	28.70	28.60	35.80
5.81	18.5	11.4	15.0	16.5	87.3	74.2	73.5	91.0
0.94	2.57	1.58	2.64	2.41	12.5	11.5	11.7	14.6
4.97	11.8	7.29	14.6	11.5	57.9	55.3	57.8	73.1
1.41	2.67	1.81	4.36	2.66	12.3	12.2	12.4	15.6
0.44	1.20	0.86	1.37	1.20	3.95	3.91	4.16	5.05
1.29	2.49	1.57	3.99	2.56	11.7	11.3	12.5	14.6

Table 1 (*continued*)

Middle Zone					Upper Zone			
VIII					IX			
SH10-30	SH10-204	SH10-32	SH10-33	SH10-71	SH10-69	SH10-68	SH10-67	SH10-65
Mass-Ore	Gb	Gb	Mt-Gb	Mt-Gb	Mt-Gb	Mt-Gb	Mt-Gb	Mt-Gb
422	413	399	384.5	343	323	297	270	239
Trace elements (ppm)								
0.19	0.34	0.20	0.58	0.30	1.26	1.27	1.37	1.57
0.91	1.62	0.95	2.97	1.42	5.60	5.52	5.81	6.42
0.16	0.28	0.17	0.53	0.25	0.98	1.00	1.00	1.09
0.42	0.71	0.37	1.16	0.57	2.16	2.17	2.33	2.48
0.05	0.08	0.05	0.14	0.07	0.25	0.22	0.23	0.24
0.30	0.47	0.27	0.85	0.38	1.42	1.12	1.12	1.22
0.04	0.07	0.04	0.11	0.06	0.21	0.15	0.15	0.16
1.54	1.62	0.95	2.26	1.13	3.31	1.53	1.46	1.15
1.23	1.11	0.54	0.54	1.13	1.50	1.04	1.01	1.28
0.18	0.72	0.26	0.29	0.33	2.82	0.53	0.53	0.75
0.03	0.17	0.06	0.07	0.10	0.68	0.08	0.12	0.14
1.73	2.54	1.13	10.10	1.86	2.16	3.85	0.89	1.10

Upper Zone									
IX		X							
SH10-64	SH10-58	SH10-57	SH10-113	SH10-114	SH10-56	SH10-55	SH10-54	SH10-52	SH10-51
Mt-Gb	Gb	Mt-Gb	Gb	Gb	Gb	Gb	Mt-Gb	Gb	Mt-Gb
221	211	179	160	141	121	89	70	30	15
Major oxides (wt.%)									
26.8	38.4	25.2	41.4	34.3	37.6	37.3	27.2	32.9	25.3
8.86	5.29	10.9	4.77	6.78	5.05	5.73	9.25	6.92	11.0
11.0	15.1	6.12	16.0	13.5	15.5	11.8	7.31	12.3	4.43
11.0	4.6	12.4	4.8	9.6	4.6	5.3	7.7	18.4	14.2
12.0	8.8	14.8	7.7	7.9	7.5	9.9	15.6	1.0	14.0
0.19	0.19	0.36	0.21	0.17	0.15	0.23	0.25	0.24	0.36
6.1	5.6	8.7	5.7	5.7	4.3	7.6	10.2	7.2	11.1
15.2	11.9	11.9	9.1	14.5	15.7	11.7	12.9	11.4	11.6
0.55	2.50	0.74	2.87	0.99	1.83	2.16	0.42	1.54	0.43
0.48	0.54	0.06	1.41	1.46	0.20	0.60	0.09	1.11	0.05
3.41	2.51	4.00	1.83	2.23	1.81	2.61	3.14	3.09	3.35
1.02	0.72	1.31	0.54	–	0.92	0.98	–	0.79	1.01
1.27	1.93	1.26	1.77	1.67	3.30	2.37	3.20	2.10	1.29
97.8	98.0	97.6	98.0	98.6	98.6	98.3	97.2	98.9	97.9
24.3	14.3	28.8	13.3	18.3	13.0	16.3	25.0	19.5	29.7
0.83	0.47	0.75	0.57	1.10	0.55	0.48	0.45	17.51	0.92
1.24	0.87	1.13	1.01	1.42	0.92	0.92	0.84	2.67	1.30
Trace elements (ppm)									
13.3	7.7	12.6	8.7	11.8	9.0	10.5	12.3	9.1	13.3
595	222	487	244	530	301	294	566	357	438
9.6	4.4	9.0	10.7	19.8	8.4	18.3	85.0	7.7	15.9
75.1	14.3	28.8	10.0	50.4	33.8	37.2	71.8	37.8	21.0
6.44	3.07	2.74	4.57	10.7	6.38	5.60	19.9	3.2	4.40
31.1	15.7	35.2	17.2	45.0	19.3	16.7	54.8	23.8	29.3
36.0	25.7	3.77	76.6	90.9	9.01	31.9	8.83	67.8	4.75
1500	3940	1610	4680	2180	1610	1480	501	2750	645
26.8	24.5	40.9	27.0	23.0	18.3	22.9	30.3	31.8	32.9
36.2	31.4	40.5	38.8	41.6	31.1	29.8	69.0	44.6	38.2
8.68	13.7	27.7	19.4	8.51	8.32	6.83	27.2	20.7	20.1
144	228	56.6	666	705	93.8	369	11.1	366	19.3
27.30	32.00	48.30	37.60	27.00	19.20	21.00	31.00	42.80	35.10
71.7	76.2	125.0	92.9	68.7	49.1	55.2	78.8	101.0	91.3
11.4	11.8	19.5	13.6	10.6	7.6	8.8	11.8	15.0	14.7
56.1	55.1	92.8	62.5	54.7	36.4	43.2	61.2	68.8	73.1
12.5	11.5	20.2	13.1	11.8	8.4	10.1	14.1	15.0	15.6
4.07	4.54	6.85	5.30	3.75	2.89	3.29	3.96	4.63	5.28
11.9	10.9	18.8	12.0	10.6	7.73	9.33	12.0	13.5	14.6
1.30	1.22	1.88	1.37	1.37	0.85	1.05	1.59	1.54	1.64
5.56	5.46	8.31	6.09	5.88	3.77	4.70	7.14	6.68	7.08
0.98	0.96	1.50	1.08	0.94	0.72	0.86	1.23	1.17	1.23
2.19	2.14	3.37	2.39	2.23	1.63	1.88	3.16	2.73	2.72
0.20	0.23	0.32	0.25	0.21	0.17	0.20	0.33	0.25	0.27
1.06	1.07	1.66	1.35	1.26	0.88	0.94	1.98	1.31	1.38
0.16	0.15	0.24	0.19	0.16	0.12	0.13	0.26	0.18	0.19
1.37	0.84	1.31	1.29	1.61	1.18	1.13	3.01	1.36	1.36
1.01	1.25	2.95	2.08	0.75	0.75	0.74	1.99	2.22	2.09

(*continued on next page*)

Table 1 (*continued*)

Upper Zone									
IX		X							
SH10-64	SH10-58	SH10-57	SH10-113	SH10-114	SH10-56	SH10-55	SH10-54	SH10-52	SH10-51
Mt-Gb	Gb	Mt-Gb	Gb	Gb	Gb	Gb	Mt-Gb	Gb	Mt-Gb
221	211	179	160	141	121	89	70	30	15
Trace elements (ppm)									
0.50	0.84	0.88	1.06	0.73	0.45	0.54	4.20	1.15	0.79
0.11	0.25	0.21	0.29	0.17	0.19	0.18	1.31	0.27	0.19
0.83	1.36	1.32	3.02	3.15	3.00	5.34	1.06	1.55	0.85

Note: Gb = Gabbro; Cpx = Clinopyroxenite; Ocp = Olivine clinopyroxenite, Mt-Gb = Magnetite gabbro; Mt-Cpx = Magnetite clinopyroxenite; Mt-Ocp = Magnetite olivine clinopyroxenite; Mass-Ore = Massive ore; LOI = Loss on ignition.

define the rocks containing 20–80% Fe–Ti oxides as disseminated ore. The magnetite exsolution lamellaes in the clinopyroxene grains are also very common in the MZ rocks (Fig. 4d). These textures suggest a crystallization sequence of olivine + Fe–Ti oxide → clinopyroxene → plagioclase → hornblende + biotite + apatite.

The MZ can be further subdivided into four cycles (V to VIII from the base to the top). The massive ore layer occurs at the base of each cycle unit and is overlain by the disseminated ore layer as Fe–Ti oxides decrease gradually (Fig. 3). The contact boundary between two cycle units is generally sharp (Fig. 4e, f), indicating that the appearance of the massive ore layer represents replenishment of a major pulse of new Fe–Ti enriched magma, similar to the situation in the Panzhihua intrusion (Song et al., 2013). The thicknesses of the massive ore and disseminated ore layers are up to 40 m and 100 m respectively in the MZ (Fig. 3). In the MZ, plagioclase appears only in the cycle unit VIII as one of cumulus minerals (Fig. 3).

3.3. Upper Zone

The UZ is characterized by abundance of apatite and consists of apatite gabbro with a few interlayers of apatite magnetite gabbro. The apatite gabbro generally contains <15 modal% Fe–Ti oxides, 20–45% clinopyroxene, 40–50% plagioclase, 5–7% apatite and <3–5% hornblende (locally up to 10%). When Fe–Ti oxide increases to 20–25%, we named it as apatite magnetite gabbro (Fig. 4g). The UZ is further subdivided into cycle units IX and X. Apatite crystals are commonly euhedral or subhedral columnar and always clearly orientated in the UZ rocks, whereas magnetite is generally interstitial between clinopyroxene, plagioclase and apatite (Fig. 4g). Magnetite exsolution lamellaes are rare in clinopyroxene crystals. These textures suggest that the Fe–Ti oxides crystallized later than silicates and apatite in the UZ.

4. Sampling and analytical methods

The samples of the three lothologic zones in this study are collected from two drill cores located in the south part of the Hongge intrusion. 42 samples (SH10-51–SH10-114) are from the bore hole ZK11003 (Fig. 2b), whereas the other 12 samples (SH10-20–SH10-33 and SH10-203) are from the other bore hole ZK13003 due to the absence of the upper part of the Middle Zone in the bore hole ZK11003 (Fig. 2b). The stratigraphic positions of these samples are shown in Fig. 3.

Major oxide analysis was completed at the ALS Laboratory Group, Mineral Division-ALS Chemex at Guangzhou. The major elements were determined by X-ray fluorescence and FeO by wet chemistry. The analyzed uncertainty is usually <5%. Trace elements were analyzed at Institute of Geochemistry, Chinese Academy of Sciences in Guiyang using a Perkin-Elmer EIAN DCR II ICP-MS. Accuracy and precision of the ICP-MS analyses are estimated to be better than 5%. Major element and trace element compositions are listed in Table 1.

Electron microprobe analyses of olivine and magnetite in this study were performed using the EMPA-1600 electron microprobe at Institute of Geochemistry, Chinese Academy of Sciences. Accelerating voltage is 25 kV, a beam current of 10 nA and a spot diameter of 10 μm were used. The detection limit for these elements under such conditions is 0.01 wt.% and analytical reproducibility was within 2%. Contents of V_2O_3 were determined by energy dispersive spectrum for 100 s. Compositions of olivine and magnetite are given in Supplementary Tables A1 and A2 respectively.

Clinopyroxene compositions have been obtained by the LA-ICP-MS at Institute of Geochemistry, Chinese Academy of Sciences operating at 4 Hz repetition rate, 160 laser pulses and a spot diameter of 60 μm. By applying normalization strategy of bulk clinopyroxene components to 100% and calibration against using USGS reference glasses as multiple reference materials, major and trace element contents of clinopyroxene can be accurately determined simultaneously (Liu et al., 2008). The calibration lines are based on BIR-1G, BHVO-2G, BCR-2G and GSE-1G. The precision of major oxides and trace elements of the clinopyroxene is generally better than 5% and 10% respectively. The compositions of clinopyroxene are listed in Supplementary Table A3.

Rb–Sr and Sm–Nd isotopic analyses of whole-rock samples were determined using on a MC–ICPMS at Guangzhou Institute of Geochemistry, Chinese Academy of Sciences. Mass fractionation corrections for Sr and Nd isotopic ratios were based on values of $^{86}Sr/^{88}Sr = 0.1194$ and $^{146}Nd/^{144}Nd = 0.7219$. The analytical errors are less than 0.005% for $^{143}Nd/^{144}Nd$ and $(^{87}Sr/^{86}Sr)_i$. Rb–Sr and Sm–Nd isotopic compositions are listed in Table 2.

5. Analytical results

5.1. Whole rock geochemistry

The LZ rocks have significantly high Cr contents relative to the MZ and UZ rocks, except for the MZ massive ores (Fig. 5a). In the cyclic units I, II and IV of the LZ, contents of Fe_2O_{3T} and Cr as well as ratios of Fe^{3+}/Fe^{2+} and Mt/(Mt + Ilm) roughly decrease upwards (Fig. 5a, b, d, e). Whereas, in the cyclic unit III, Cr decreases as Fe_2O_{3T} increases upwards (Fig. 5a, b), and ratios of Fe^{3+}/Fe^{2+} and Mt/(Mt + Ilm) vary irregularly (Fig. 5d, e).

For the MZ, whole rock Fe_2O_{3T} and Cr contents as well as ratios of Fe^{3+}/Fe^{2+} and Mt/(Mt + Ilm) decrease regularly from the base to the top in each cycle unit (Fig. 5a, b, d, e). The massive ores contain as high as 55–70 wt.% Fe_2O_{3T} and 15–25 wt.% TiO_2; and the disseminated ores contain 20–55 wt.% Fe_2O_{3T} and 5–18 wt.% TiO_2 (Table 1 and Fig. 5b). The massive ores have the highest whole-rock Cr contents due to extremely high contents of magnetite, which has high partition coefficient of Cr relative to basaltic liquid ($D_{Cr}^{Mt/Liquid} = 153$, Rollinson, 1993). Comparing with the MZ and LZ, the UZ rocks are characterized by obviously high P_2O_5 and low Cr contents (Fig. 5a, c).

Table 2
Sr–Nd isotopes of the Hongge intrusion.

Zone	Cycle	Sample	Rock type	Depth (m)	Sm (ppm)	Nd (ppm)	$^{143}Nd/^{144}Nd$	(2σ)	$(^{143}Nd/^{144}Nd)_{259}$	εNd(t)	Rb (ppm)	Sr (ppm)	$^{87}Sr/^{86}Sr$	(2σ)	$(^{87}Sr/^{86}Sr)_{259}$
Wallrock		SH10-73	Wallrock	1047	3.91	25.3	0.511855	0.000009	0.511697	−11.86	221	206	0.729027	0.000013	0.717568
		SH10-74	Wallrock	1028	5.18	30.07	0.511806	0.000010	0.511630	−13.17	179.72	163.57	0.726686	0.000016	0.714953
Lower Zone	I	SH10-75	Mt-Ocp	1017	2.94	12.8	0.512452	0.000008	0.512217	−1.71	42.9	107	0.710804	0.000011	0.706529
		SH10-77	Mt-Ocp	988	2.5	10.7	0.512516	0.000009	0.512277	−0.54	7.54	165	0.706394	0.000016	0.705907
	II	SH10-91	Ocp	792	2.65	9.32	0.512573	0.000010	0.512282	−0.44	2.33	88.6	0.706001	0.000014	0.705721
		SH10-94	Mt-Ocp	760	3.41	11.6	0.512534	0.000007	0.512233	−1.40	7.31	93.6	0.706994	0.000011	0.706162
	IV	SH10-96	Ocp	735	3.48	10.6	0.512637	0.000010	0.512301	−0.07	34.1	135	0.709026	0.000013	0.706333
		SH10-100	Cpx	692	5.73	21.5	0.512433	0.000012	0.512160	−2.82	8.08	459	0.707758	0.000013	0.707570
Middle Zone	VI	SH10-72	Mt-Cpx	596	3.06	11.3	0.512607	0.000011	0.512330	0.49	14	117	0.707527	0.000013	0.706252
	VII	SH10-24	Mt-Cpx	503	2.9	10.1	0.512582	0.000009	0.512288	−0.32	2.35	81.7	0.706444	0.000016	0.706137
		SH10-26	Mt-Cpx	462	9.64	42.8	0.512381	0.000009	0.512150	−3.01	24.1	91.8	0.709457	0.000013	0.706658
	VIII	SH10-204	Gb	413	2.67	11.8	0.512526	0.000010	0.512294	−0.20	93.7	1670	0.706416	0.000018	0.705818
Upper Zone	IX	SH10-69	Mt-Gb	323	12.3	57.9	0.512495	0.000009	0.512277	−0.53	21.6	1160	0.706235	0.000016	0.706037
		SH10-68	Mt-Gb	297	12.2	55.3	0.512505	0.000008	0.512279	−0.50	0.954	1460	0.706072	0.000010	0.706065
		SH10-65	Mt-Gb	239	15.6	73.1	0.512473	0.000011	0.512254	−0.98	1.62	1720	0.705941	0.000011	0.705931
		SH10-64	Mt-Gb	221	12.5	56.1	0.512505	0.000010	0.512277	−0.54	36	1500	0.706015	0.000011	0.705759
	X	SH10-54	Mt-Gb	70	14.1	61.2	0.512513	0.000009	0.512277	−0.54	8.83	501	0.706032	0.000014	0.705844

Note: Gb = Gabbro; Cpx = Clinopyroxenite; Ocp = Olivine clinopyroxenite, Mt-Gb = Magnetite gabbro; Mt-Cpx = Magnetite clinopyroxenite; Mt-Ocp = Magnetite olivine clinopyroxenite; Mass-Ore = Massive ore.

As shown in Fig. 6a, TiO_2 contents of the Hongge samples, similar to the rocks of the Panzhihua intrusion, are well positively correlated with Fe_2O_{3T}. Most of the LZ and MZ samples have lower TiO_2 contents relative to the UZ samples at the comparable Fe_2O_3 contents (Fig. 6a). The contents of P_2O_5 of the UZ rocks of both the Hongge and Panzhihua intrusions are comparable, whereas the MZ and LZ samples of the Hongge intrusion are slightly higher in P_2O_5 than those of the Panzhihua intrusion (Fig. 6b). Fig. 6c displays perfectly positive correlation between V and Fe_2O_{3T}, indicating that magnetite is the main phase containing V. Fig. 6d shows that the Hongge LZ rocks have obviously higher Cr contents than the MZ and UZ rocks and the Panzhihua rocks at the comparable Fe_2O_{3T} contents. The whole rock Cr contents are positively correlated with Fe^{3+}/Fe^{2+} ratios for the MZ rocks, whereas no similar correlations display in the LZ and UZ rocks (Fig. 6e). Positive correlation between P_2O_5 and REE_{Total} contents indicates that apatite is the main phase containing rare earth elements (REE) because of their high apatite/silicate melt partition coefficients ($D_{REE}^{Ap/Liquid} = 1–5$, Prowatke and Klemme, 2006) (Fig. 6f).

As shown in Fig. 7, the Hongge samples plot in the area of oceanic island basalt (OIB) and have much narrower ranges of εNd_{259Ma} and $(^{87}Sr/^{86}Sr)_{259Ma}$ values than the high-Ti Emeishan basalts. All of the Hongge rocks display lower εNd_{259Ma} and higher $(^{87}Sr/^{86}Sr)_{259Ma}$ values than the rocks of the Panzhihua, Taihe and Baima intrusions, indicating higher degree of crustal contamination (Fig. 7). Moreover, the LZ samples display variable values of εNd_{259Ma} and $(^{87}Sr/^{86}Sr)_{259Ma}$, ranging from −2.82 to −0.07 and from 0.7057 to 0.7076, respectively, whereas the MZ and UZ samples have relatively small variation in εNd_{259Ma} and $(^{87}Sr/^{86}Sr)_{259Ma}$ values (Table 2 and Fig. 7). The footwall metasandstones have much lower εNd_{259Ma} (−11.86 to −13.17) and higher $(^{87}Sr/^{86}Sr)_{259Ma}$ values (0.7150–0.7177) than these layered intrusions.

5.2. Mineral compositions

Consistent with the whole-rock compositional variations, compositions of clinopyroxene and olivine also show reversals in the cycle units. For the cyclic units of the LZ and MZ, Cr and Ni contents of clinopyroxene as well as Mg# of Cpx decrease upwards roughly, although reversed variations appear in the cyclic unit I (Fig. 5f, g, h). Ni contents of olivine decrease upwards in each cycle unit as well (Fig. 5i).

As shown in Fig. 8a, the Cr contents of both clinopyroxene and magnetite decrease from the LZ through the MZ to the UZ. Although there is a positive correlation between the Cr contents of the two minerals, Cr content of the magnetite is higher than that of the clinopyroxene in the same sample (Fig. 8a). Thus, the perfectly positive correlation of Cr contents between magnetite and whole-rock indicates that the magnetite is the dominant mineral containing Cr (Fig. 8b). The LZ olivine crystals are higher in Ni contents than those of the MZ and much higher than the Panzhihua olivine (Song et al., 2013), although their forsterite contents (Fo) are lower (Supplementary Table A1 and Fig. 8c). Fig. 8d shows a positive correlation between the Cr and Ni contents of the clinopyroxene in the LZ and MZ. Both the clinopyroxene and magnetite of the MZ and LZ of the Hongge intrusion have much higher Cr and Ni contents than those of the UZ as well as those of the Panzhihua intrusion (Figs. 8d, e) (Song et al., 2013). As shown in Fig. 8f, Zr and La contents of the clinopyroxene of the LZ and MZ are positively related, whereas, La contents of the clinopyroxene in the UZ display a small variation. Moreover, the Zr and La contents in clinopyroxene are similar to those of whole rock in the LZ and MZ, suggesting that clinopyroxene is the main mineral containing the incompatible elements in the LZ and MZ rocks. The UZ rocks have high La contents relative to the clinopyroxene due to accumulation of apatite.

6. Discussion

Crystallization experiments of tholeiitic magmas indicated that both primarily high contents of Fe_2O_{3T} and TiO_2 in the magma and

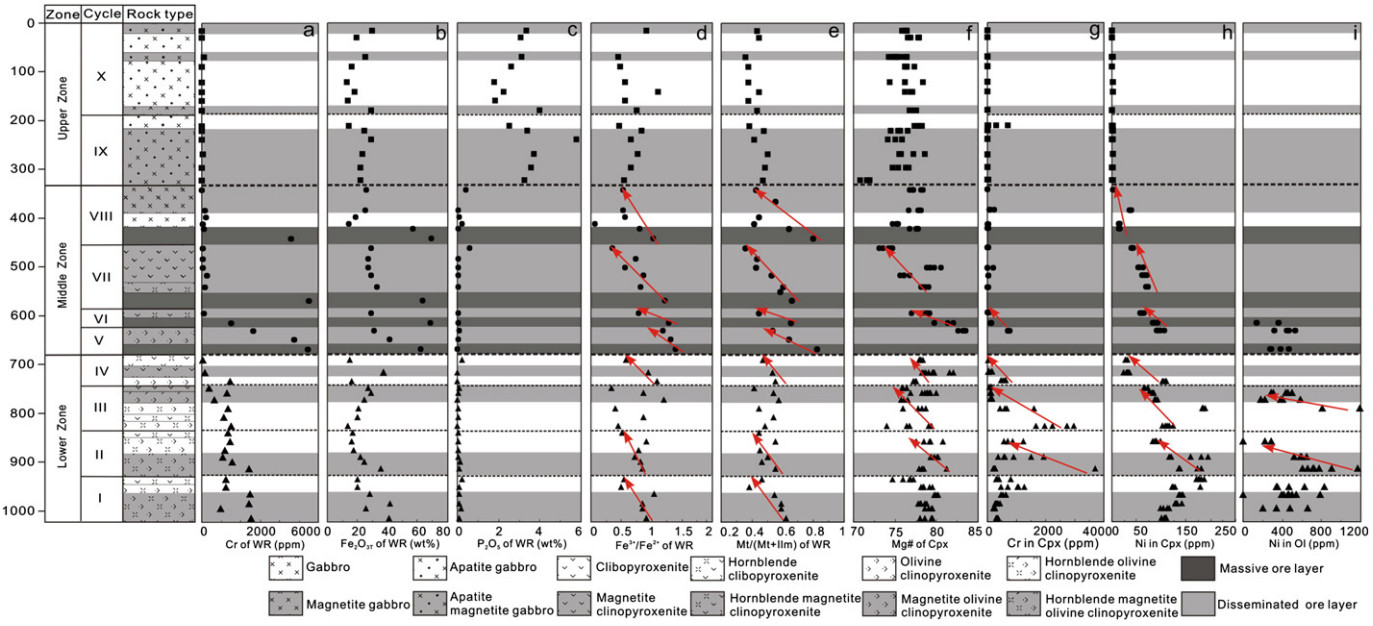

Fig. 5. Stratigraphic variations of the Hongge whole-rock Cr contents (a), Fe_2O_{3T} (b), P_2O_5 (c), Fe^{3+}/Fe^{2+} rations (d) and Mt/(Mt + Ilm) (e), Mg#, Cr and Ni contents of clinopyroxene (f, g and h, respectively), and Ni contents of olivine (i). WR = whole rock; Cpx = clinopyroxene; Ol = olivine.

elevation of f_{O2} are critical for early crystallization of Fe–Ti oxides (Berndt et al., 2005; Botcharnikov et al., 2008). Ganino et al. (2008) proposed that interaction between the CO_2 degassed from footwall limestone and the magma probably resulted in elevation of f_{O2} and early crystallization of magnetite in the Panzhihua intrusion. The most recent studies have demonstrated that the early crystallization and accumulation of the Fe–Ti oxides in the Panzhihua intrusion were attributed to high contents of Fe_2O_{3T} and TiO_2 in the Fe–Ti enriched magmas due to fractional crystallization of olivine and clinopyroxene at depth (Song et al., 2013).

For the Hongge intrusion, although the euhedral magnetite enclosed in clinopyroxene indicates early crystallization of the magnetite in the LZ, the massive oxide ore layers occur in the MZ. Assimilation of the footwall limestone might result in significant elevation of f_{O2} and early crystallization of the Fe–Ti oxides in the Hongge intrusion (Bai et al., 2012), whereas this hypothesis cannot explain that why massive Fe–Ti oxide ore layers formed in the MZ rather than in the LZ. Our observations indicate that the bases of the Hongge intrusion not only contact with limestones, but also with meta-sandstones, at least in the exploration line including the bore hole sampled in this study (see above description and Table 1 and Fig. 2b). This implies that assimilation of the limestone may be not the critical factor for the early crystallization and accumulation of the Fe–Ti oxides in the Hongge intrusion. Thus, the three major issues, (1) what is the compositional difference of the parental magmas of the three zones, (2) why Fe–Ti oxides crystallized early in the LZ, (3) why and how extensive accumulation of Fe–Ti oxides was formed in the MZ, remain poorly understood and unexplained.

6.1. Early magnetite crystallization in the LZ

6.1.1. More primitive parental magma

Although the composition of the parental magma of the Hongge intrusion is difficult to be estimated because of the absence of chilled margin, olivine and clinopyroxene as early crystallized minerals can be used to speculate the compositional features of the parental magma (Driouch et al., 2010). Clinopyroxene and olivine of the LZ commonly have high Cr and Ni contents relative to those of the MZ and UZ, respectively (Supplementary Tables A1 and A3, Figs. 5g, h, i and 8c, d), demonstrating that the parental magmas of the LZ are higher in Cr and Ni contents and more primitive than those of the other two zones. The data compiled in Table 3 clearly indicates that, at the timing of oxides saturation, the LZ parental magmas of the Hongge intrusion were able to crystallize more primitive olivine and clinopyroxene than other layered intrusions, such as the Bushveld Complex and the Skaergaard intrusion. The enrichment of Cr and Ni in the parental magma also caused relatively high Cr_2O_3 and NiO contents in the magnetites of the LZ (Supplementary Table A2 and Fig. 8e). The reversals on the Mg# as well as Cr and Ni contents of the clinopyroxene in the four cycle units of the LZ suggest that there are several pulses of magmas with variable compositions intruding into the Hongge intrusion during the formation of the LZ (Fig. 5f, g, h).

6.1.2. Crustal contamination and introduction of external H_2O

The Sr–Nd isotope values of the Hongge intrusion indicate more extensive crustal contamination than the Panzhihua, Baima and Taihe intrusions (Fig. 7). Moreover, more extensive crustal contamination leads to the LZ rocks having lower εNd_{259Ma} and higher $(^{87}Sr/^{86}Sr)_{259Ma}$ values than the MZ and UZ rocks (Fig. 7). If the primary magma has Sr–Nd isotope composition of the Emeishan picrite ($\varepsilon Nd(t) = +7$ and $(^{87}Sr/^{86}Sr)_i = 0.704$, Wang et al., 2007) and the contaminant is the meta-sandstone, which is the footwall rock of the Hongge intrusion, the degree of the contamination of the LZ rocks is probably up to ~10–15% (Fig. 7). Because the Hongge samples are not plotted between the Emeishan picrite and the Yangtze lower crust (Fig. 7), we speculate that the crustal contamination dominantly occurred in a shallow depth, more likely when the magma entered the Hongge intrusion. Fig. 9 again indicates that stronger contamination of wallrocks resulted in the parental magmas in equilibrium with the clinopyroxene of the LZ having low $(Nb/Th)_{PM}$ but high $(Th/Yb)_{PM}$ ratios relative to those of the MZ and UZ.

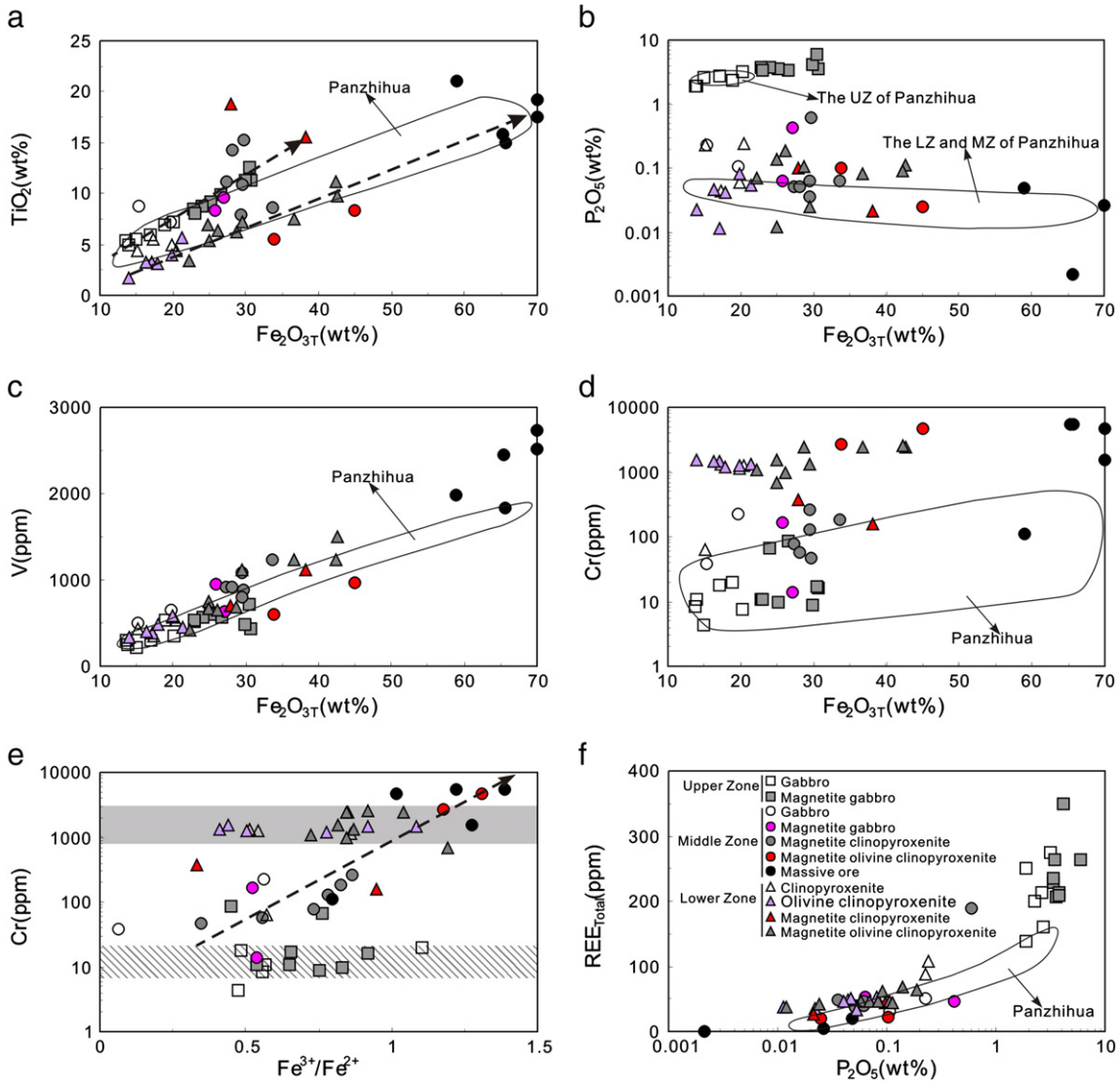

Fig. 6. Whole-rock binary plots of Fe_2O_{3T} vs. TiO_2 (a), Fe_2O_{3T} vs. P_2O_5 (b), Fe_2O_{3T} vs. V (c), Fe_2O_{3T} vs. Cr (d), Fe^{3+}/Fe^{2+} vs. Cr (e), P_2O_5 vs. REE_{Total} (f). The area of the rocks of the Panzhihua intrusion is after Song et al. (2013).

Experiments have demonstrated that the addition of water could decrease liquidus and solidus temperatures of basaltic magma and change significantly the sequence of crystallizing mineral phase (Botcharnikov et al., 2008; Feig et al., 2006, 2010; Gaetani et al., 1993). These experimental investigations indicated that the increase of H_2O contents can result in crystallization of clinopyroxene before plagioclase and early crystallization of magnetite. Thus, the absence of cumulus plagioclase and the presence of abundance of hornblende in the LZ rocks suggest that the parental magma was originally hydrous. Experimental studies have indicated that crystallization of hornblende needs 2–3 wt.% H_2O in the magma (Foden and Green, 1992; Stone et al., 1997). The rocks of the layered intrusions in the ELIP, such as the Panzhihua and Baima intrusions, commonly contain less than 2 modal% interstitial hornblende (Song et al., 2013; Zhang et al., 2012). Recent studies suggested that ~2% interstitial hornblende of the Panzhihua gabbros was crystallized from H_2O-enriched interstitial liquid after extensive crystallization of silicates and oxides (Howarth and Prevec, 2013; Howarth et al., 2013). However, ~5–15% poikilitic hornblende in the Hongge LZ indicates that the LZ parental magma contained much more H_2O content than the Panzhihua intrusion and contents of H_2O in the residual magma reached to 2–3 wt.% when hornblende crystallized. Very low contents of plagioclase in the LZ also suggest that the mineral accumulation occurred before extensive crystallization of plagioclase. MELT calculation indicates that the parental magma of the LZ should contain at least 1.5 wt.% H_2O, so that the water content in the residual magma can reach to 2.0 wt.% before crystallization of plagioclase (see below). However, the primary mantle derived magmas (MORB) generally have low H_2O content (<0.51 wt.%) (Sobolev and Chaussidon, 1996) and the parental magma of the Siberin LIP contained less than 0.25 wt.% water (Sobolev et al., 2009), which is consistent with their previous studies. The recent study of the melt inclusions in olivine phenocrysts of Emeishan picrites indicated a very low volatile concentration of the primary picritic magmas of the Emeishan plume (Kamenetsky et al., 2012). Therefore, it is presumed that the parental magmas of the Hongge intrusion derived from the Emeishan mantle plume contain much lower than 0.25 wt.% water. It is hard for H_2O content in residual liquid to increase to 2–3 wt.% before crystallization of plagioclase only via fractionation of such magma. Thus, it is obvious that external water was introduced into the Hongge intrusion during the assimilation of the footwall meta-sandstone.

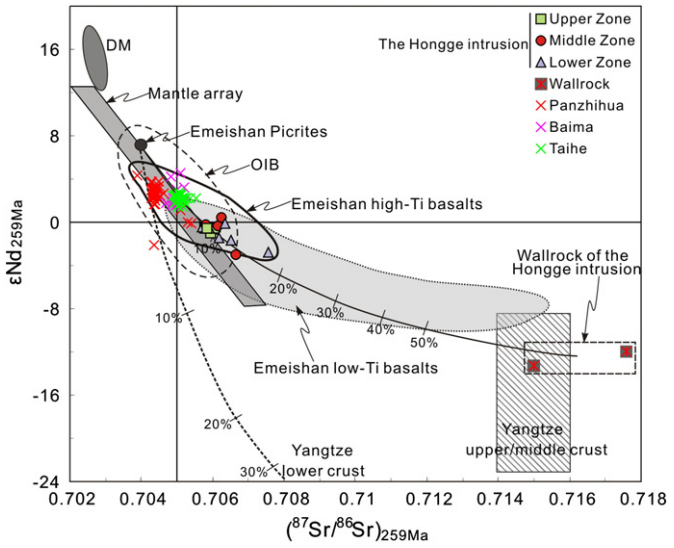

Fig. 7. Binary plots of εNd_{259Ma} vs. $(^{87}Sr/^{86}Sr)_{259Ma}$ in the Hongge intrusion. DM (depleted mantle) and mantle array are after Zindler and Hart (1986). The calculated parameters of Nd (ppm), εNd(t), Sr (ppm) and $(^{87}Sr/^{86}Sr)_i$ are 4.4, +7, 102 and 0.704 from picrites in northern Vietnam as primary magmas (Wang et al., 2007). The Yangtze upper/middle and lower crust data are from Chen and Jahn (1998). Panzhihua data are after Zhou et al. (2008), Zhang et al. (2009) and Song et al. (2013); Baima data are after Zhou et al. (2008); Taihe data are after She et al. (2014). Emeishan high-Ti and low-Ti basalts date are from Xu et al. (2001), Xiao et al. (2003, 2004), Zhou et al. (2006) and Song et al. (2008a).

6.1.3. Early crystallization of magnetite — insights from MELTS calculation

The euhedral magnetite crystals enclosed in clinopyroxene in the LZ indicate early crystallization of magnetite (Fig. 4a). Experimental studies by Baker and Rutherford (1996) and Gaillard et al. (2001) indicated that dissolved water has a specific positive effect on the Fe^{3+}/Fe^{2+} ratio of the silicic melts when oxygen fugacity (f_{O2}) is less than NNO + 1 (≈FMQ + 1.7), although f_{O2} of the melts has small variation. The common appearance of sulfide and the absence of sulfate in the Hongge intrusion demonstrated f_{O2} < FMQ + 1.8 (Jugo et al., 2005). This suggests a potential relationship between the early crystallization of the Fe–Ti oxide in the LZ and elevation of Fe^{3+}/Fe^{2+} ratio of the magma due to introduction of H_2O during assimilation of the wallrock. However, although magnetite crystallized early, only disseminated ore layers developed in the LZ of the Hongge intrusion.

As shown in Fig. 10, the parental magmas in equilibrium with clinopyroxene of the Hongge intrusion display similar trace element patterns with the Emeishan high-Ti basalts, indicating a genetic linkage between them. This is consistent with the recent studies, which demonstrated that the layered intrusions in the ELIP are associated with high-Ti basaltic magma (Song et al., 2005; Zhou et al., 2008). Thus, we assume that the primary magma of the Hongge intrusion had a composition similar to the melt inclusion (M8 62) hosted in high Fo olivine phenocrysts (Fo = 91.71) of the Emeishan high-Ti picrite (Kamenetsky et al., 2012). The melt inclusion contains 12.29 wt.% FeO_T, 19.68 wt.% MgO and 2.25 wt.% TiO_2. We use the MELTS package modified by Ghiorso and Sack (1995) to model the hidden fractionation of the H_2O-free picritic melt under f_{O2} of FMQ in the deep-seated magma chamber (~5 kbar).

MELTS calculation indicates that at 5 kbar, olivine is the first phase to appear on the liquids (Fo = 91 at 1476 °C), followed by spinel and pyroxenes (Fig. 11a, b). The olivine has high Fo (91–86) and spinel is high in Cr_2O_3 (up to 47.0 wt.%), which are consistent with the mineral composition of the high-Ti picrites (Kamenetsky et al., 2012). Crystallization of these minerals gives rise to a residual magma gradually enriching in Fe_2O_{3T} and TiO_2 (Fig. 11a, b). When the temperature decreases to ~1230 °C after fractional crystallization of ~15.6% olivine, ~0.70% spinel, ~9.0% orthopyroxene and ~23.8% clinopyroxene, the Fe_2O_{3T} and TiO_2 contents in the residual liquid increase to ~18.2 wt.% and 4.27 wt.%, respectively (Fig. 11a, b).

If such magma was squeezed from the deep-seated chamber and injected into the Hongge intrusion and assimilated by 10% of the footwall meta-sandstone as indicated by the Sr–Nd isotope values (Fig. 7), Fe_2O_{3T} and TiO_2 contents of the magma decrease to 16.29 wt.% and 3.76 wt.%, respectively (Fig. 11c, d). Previous studies have demonstrated that the thickness of the Emeishan flood basalt in the area near the Hongge intrusion is ~3800 m (Mei et al., 2003; Qi et al., 2008). Thus, we predict that solidification of the Hongge intrusion occurred in a shallow depth less than 3800 m (~1 kbar) because the intrusion contacts with the Emeishan flood basalts at the northeastern corner (Fig. 2a), although we cannot know the exact depth. Basaltic magma is able to dissolve amount of water because of its as high as ~3.5 wt.% H_2O solubility at ~1 kbar (Berndt et al., 2002; Botcharnikov et al., 2005; Dixon et al., 1995; Lesne et al., 2011). The high percentage of original hornblende (~5–15%) in the LZ rocks suggests that a small amount of water was introduced into the parental magma during assimilation of the mica-bearing meta-sandstone. MELT calculation indicates that crystallization of olivine (1177 °C) is followed by magnetite (1165 °C) and clinopyroxene (1106 °C) in the shallow chamber. The poikilitic euhedral magnetite crystals within the clinopyroxenes in the LZ rocks (Fig. 4a) are accordant with the above MELT calculation. Crystallization of plagioclase is postponed to 1059 °C because of dissolved water in the magma. Early crystallization and accumulation of Fe–Ti oxides resulted in rapid decreases of Fe_2O_{3T} and TiO_2 in the magma, as well as negative Nb anomalies of the magma in equilibrium with the clinopyroxene (Fig. 10a, b), because Nb is much more compatible to ilmenite ($D_{Nb}^{Ilm/Liquid}$ = 2.3, Green and Pearson, 1987; $D_{Nb}^{Cpx/Liquid}$ = 0.005, Rollinson, 1993). The MELTS calculated compositions of olivine (Fo = 74–79) and clinopyroxene (Mg# =77–81) are well matched with those measured by electron microprobe ($Fo_{72–78}$ and $Mg\#_{76–80}$, respectively) (Supplementary Tables A1 and A3). However, when temperature decreases to 1080 °C, H_2O content in the residual liquid has already reached to ~2.02 wt.% (Fig. 11d) which is enough for hornblende crystallization (Foden and Green, 1992; Stone et al., 1997). The percentage of crystallized magnetite before 1080 °C in the LZ is only 9.6, which is much lower than that of the MZ (19.2%, see discussion below), resulting in appearance of only disseminated ore layers in the bottom of the LZ. If only 1.5 wt.% H_2O was introduced into the magma from the deep level without assimilation of the meta-sandstone, MELTS calculation predicts a crystallization sequence of olivine (1164 °C), magnetite (1157 °C), clinopyroxene (1116 °C) and plagioclase (1062 °C), which is quite similar to the above model results (Fig. 11c, d). This indicates that the occurrence of H_2O has an evident effect on the crystallization sequence, consistent with the experimental studies of Berndt et al. (2005) and Botcharnikov et al. (2008).

MELTS calculations indicate, however, that if the magma from the deep-seated magma chamber was neither assimilation of the meta-sandstone nor introduction of H_2O, crystallization of magnetite (1150 °C) would be later than silicates, including olivine (1184 °C), plagioclase (1166 °C) and clinopyroxene (1152 °C). If the magma from deep level was only assimilated by 10% of the meta-sandstone without introduction of H_2O, magnetite could crystallize at 1176 °C after olivine (1199 °C) and before plagioclase (1152 °C) and clinopyroxene (1138 °C). These results are obviously contrary to the lithological features of the LZ rocks demonstrated above. Thus, we conclude that introduction of H_2O played a key role in the early crystallization and accumulation of magnetite in the LZ, although assimilation of the footwall rock promoted the early crystallization of magnetite as well.

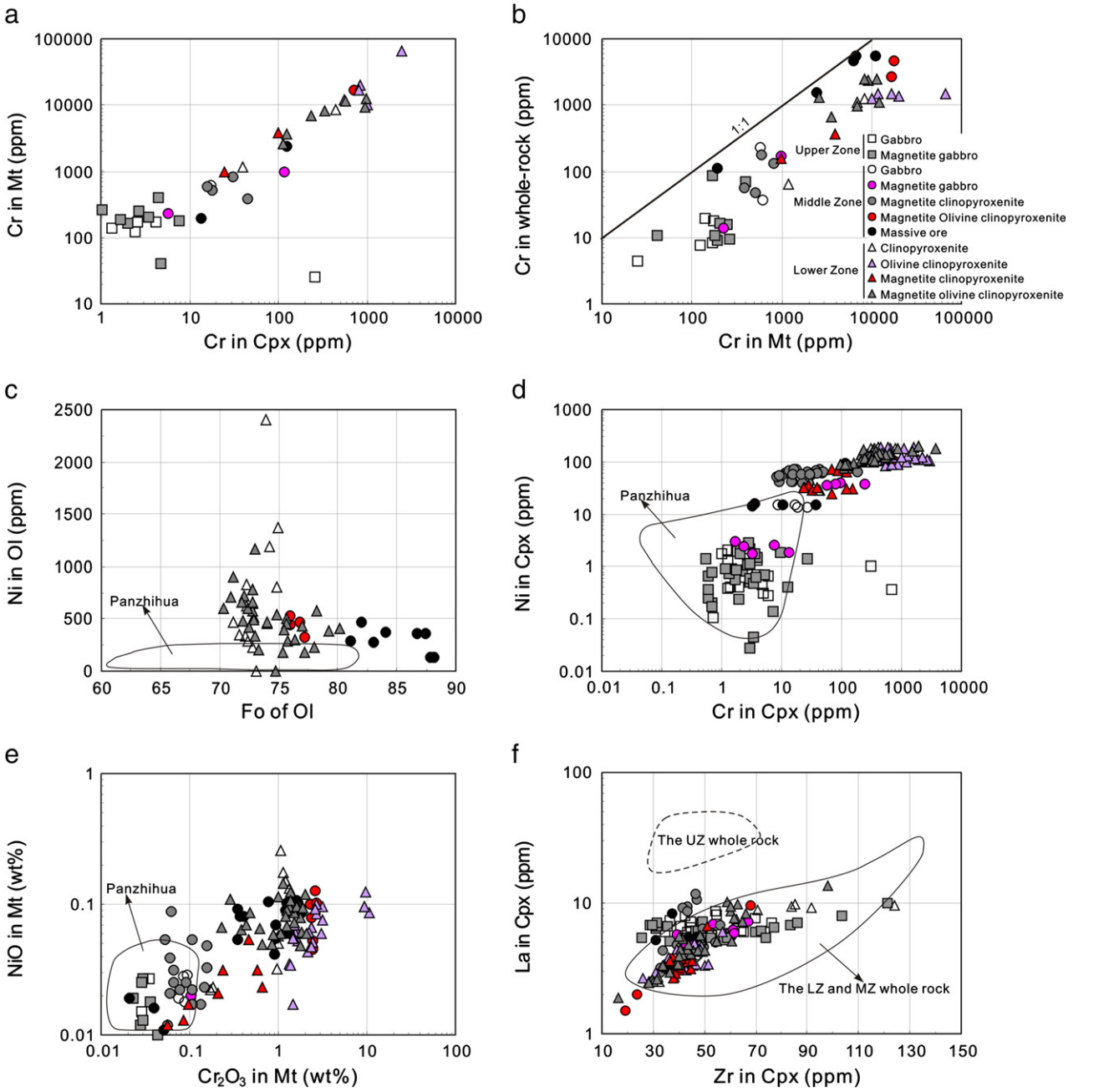

Fig. 8. Plots of the mineral compositions of the Hongge intrusion. a: Magnetite Cr vs. clinopyroxene Cr; b: magnetite Cr vs. whole-rock Cr; c: Fo vs. Ni of olivine; d: Cr vs. Ni of clinopyroxene; e: Cr_2O_3 vs. NiO of magnetite; f: Zr vs. La of clinopyroxene. Olivine and magnetite data of the Panzhihua intrusion are from Song et al. (2013).

6.2. Formation of the Fe–Ti oxide ore layers in the MZ

Compared with the LZ, the MZ is characterized by much higher Fe–Ti oxide contents at the bases of each cyclic unit (Fig. 3), but lower Cr and Ni contents of the clinopyroxene (Fig. 5g, h) and lower hornblende contents (generally <3%). Relatively high εNd_{259Ma} and low $(^{87}Sr/^{86}Sr)_{259Ma}$ and $(Th/Yb)_{PM}$ ratios indicate a relatively weak assimilation of the footwall meta-sandstone (Figs. 7, 9). The two MZ samples having high $(Th/Yb)_{PM}$ ratios (27.0–44.4) suggest magma mixing between the new injected magma and the residual contaminated magma of the LZ in the Hongge intrusion.

6.2.1. More evolved Fe–Ti enriched parental magma

The lower Cr and Ni contents in clinopyroxene of the MZ (Figs. 5g, h and 8d) indicate that the parental magma of the MZ has subjected higher degree of fractional crystallization of olivine, spinel and pyroxenes than that of the LZ before it intruded into the Hongge intrusion. This is also supported by the low Ni contents in olivine of the MZ relative to that of LZ (Figs. 5i, 8c). Fe–Mg exchange between olivine and Fe–Ti oxides resulted in the extremely high Fo of some olivine crystals (Fo = 81–88) in the massive oxides of the MZ (Supplementary Table A1 and Fig. 8c) (Frost, 1991; Frost et al., 1988). Experimental studies proposed that high FeO contents in the silicate melts may promote CaO enrichment of the crystallized olivine (Jurewicz and Watson, 1988; Libourel, 1999). The higher CaO contents in olivine of the MZ (0.1–0.22 wt.%) than that of the LZ (generally lower than 0.08 wt.%) (Supplementary Table A1) demonstrate that the parental magma of the MZ is more Fe-enriched. Additionally, the dense magnetite exsolution lamellaes in the clinopyroxene of all types of the MZ rocks (Fig. 4d) also indicate a Fe–Ti-enriched parental magma. Therefore,

Table 3
Compositions of olivine, Ca-rich pyroxene and plagioclase at the appearance of cumulus Fe–Ti oxides in several layered intrusions.

	Skaergaard[1] (Greenland)	Bushveld[1] (S. Africa)	Sept Iles MCU1[2] (Quebec, Canada)	Kiglapait[1] (Labrador, Canada)	Panzhihua[1] (SW China)	Baima[3] (SW China)	Taihe[4] (SW China)	Hongge LZ[a] (SW China)
Fo% (olivine)	40	–	66	60	71	72–74	68	74
Mg# (clinopyroxene)	55	62	–	68–71	79	–	77	80
An% (plagioclase)	46	61	61	53	69	58–67	78	53

1: Pang et al., 2009 and reference in; 2: Namur et al., 2010; 3: Zhang et al., 2012; 4: She et al., 2014. Olivine, clinopyroxene and plagioclase compositions of the Baima intrusion are from magnetite troctolites (BJ08, BJ11 and BJ21). Clinopyroxene and plagioclase compositions of the Taihe intrusion are from magnetite olivine gabbros (ST11-40) and olivine composition from olivine apatite magnetite clinopyroxenites (ST11-28). a: Olivine and clinopyroxene and those of the Hongge intrusion are from hornblende magnetite olivine clinopyroxenites (SH10-78) and plagioclase composition from magnetite olivine clinopyroxenites (SH10-93) (unpublished).

the parental magmas in equilibrium with the clinopyroxene of the MZ rocks have apparent positive Ti anomalies relative to that of the other two zones (Fig. 10c, d).

6.2.2. Formation of the massive ore layers in the MZ

We infer that the more evolved and Fe–Ti enriched parental magmas of the MZ were produced by fractional crystallization of ~15.6% olivine, ~0.9% spinel, ~9.0% orthopyroxene and ~31.1% clinopyroxene until ~1200 °C and contain ~19.5 wt.% Fe_2O_{3T} and ~4.7 wt.% TiO_2 according to MELTS modeling (Fig. 11a, b). Owing to the low contents of interstitial hornblende (generally <3%) in the MZ, we assume that the parental magmas contain a low water content (~0.8 wt.%), due to mixing of the residual water-bearing magma of the LZ.

In the shallow Hongge intrusion (1 kbar), MELTS calculations indicate that magnetite crystallizes at 1152 °C followed by olivine (1138 °C), clinopyroxene (1121 °C) and then plagioclase (1114 °C) from the more evolved and Fe–Ti enriched parental magma (Fig. 11e, f). The modeled compositions of clinopyroxene ($Mg\#_{76–81}$) and magnetite (Cr_2O_3 <0.13 wt.%) are well matched with those measured by electron microprobe (Supplementary Table A2 and A3). Because of the absence of cumulate apatite in the MZ, we assume that the magma recharge during the formation of the MZ commonly occurred before crystallization of apatite. The percentage of crystallized magnetite is up to 19.2% before the residual magma reaches saturation of apatite. If the proportion of the residual magma of the LZ is less than 40%, the parental magma will contain >15.75 wt.% Fe_2O_{3T}, >3.66 wt.% TiO_2 and ~0.8 wt.% H_2O, respectively, and magnetite will remain to crystallize early together with olivine. Thus, the magma mixing resulted in the synchronous accumulation of olivine and magnetite in cycle unit V at the base of the MZ (Fig. 3). However, the influence of the residual magma was weakened gradually, so that early crystallized magnetite mainly accumulated together with clinopyroxene in cycle units VI, VII and VIII as indicated by MELTS modeled result (Fig. 11e, f).

The most recent study by Song et al. (2013) demonstrated that the formation of thick massive Fe–Ti oxide ore layers in the Lower Zone of the Panzhihua intrusion depends not only on early crystallization of the Fe–Ti oxides, but also on gravitational resorting and setting of the Fe–Ti oxides during flowing of the frequently replenished Fe–Ti enriched magma along the base of the magma chamber. In the Hongge MZ, the abrupt contact between two cyclic units in the MZ (Fig. 4e, f) and reversion of mineral composition (Fig. 5f, g, h, i) demonstrated replenishment of multiple pulses of magma. For each pulse of Fe–Ti enriched replenished magma, magnetite is always the early crystallized mineral as the MELTS modeling. Coupling of early crystallization of large amount of magnetite and gravitational resorting and settling resulted in the formation of not only the massive oxide ore layers, but also the magnetite clinopyroxenite layers since clinopyroxene crystallized slightly later than magnetite (Fig. 3). Thus, whole-rock Fe^{3+}/Fe^{2+} and Mt/(Mt + Ilm) ratios decrease upwards in each cycle unit (Fig. 5d, e). The peaks of whole-rock Cr contents in the massive ore layers (Fig. 5a) are attributed to very high contents of magnetite, although Cr_2O_3 content in the MZ magnetite is lower than the LZ magnetite (Supplementary Table A2 and Fig. 8e). The positive correlation between Cr and Fe^{3+}/Fe^{2+} in whole rock also demonstrates that Cr contents are related to the percentage of magnetite in whole rock of the MZ (Fig. 6e). Plagioclase may float upward because of its lower density (2.64–2.67 g/cm^3) relative to the magma (~2.75 g/cm^3). Thus, plagioclase is absent in cycle unit V, VI and VII and present within cycle unit VIII of the MZ (Fig. 3).

6.3. Formation of the UZ

The UZ is marked by an abrupt increase of apatite and shows a series of distinguishable chemical features, particularly very high P_2O_5 and REE contents (Figs. 5c, 6f, 10e, f). The lowest Cr contents in the clinopyroxene and magnetite of the UZ (Figs. 5g, 8a) demonstrate that the parental magma of the UZ has experienced the most extensive fractional crystallization. The high values of εNd_{259Ma} and $(Th/Yb)_{PM}$ demonstrate that the parental magma of the UZ has experienced weak crustal contamination (Figs. 7, 9). Furthermore, the parental magma in equilibrium with the clinopyroxene of the UZ displays negative Ti anomalies compared with the LZ and MZ of the Hongge intrusion as well as the Emeishan high-Ti basalts (Fig. 10e, f), interpreting that the parental magma of the UZ was Fe–Ti-depleted due to the extensive crystallization of Fe–Ti oxides in the LZ and MZ. These distinctive features imply that the UZ was formed under a different environment.

Phosphorus is strongly incompatible to silicate minerals and Fe–Ti oxides (Bindeman et al., 1998; Jones, 1995) and is thus concentrated in the residual magma before crystallization of apatite. The

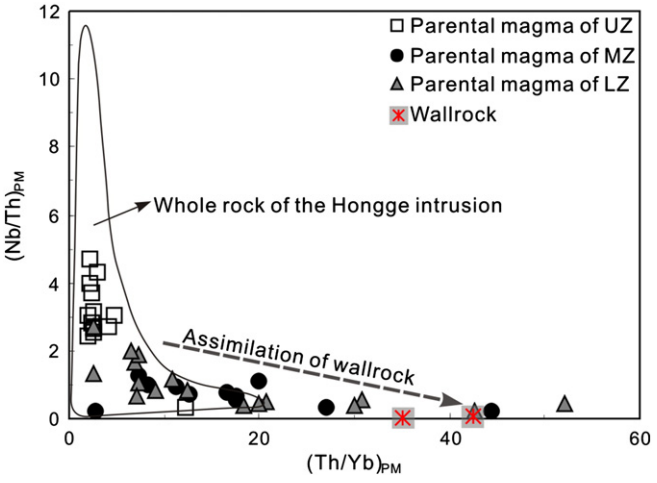

Fig. 9. Binary plots of $(Th/Yb)_{PM}$ vs. $(Nb/Th)_{PM}$ rations of the parental magmas in equilibrium with the clinopyroxene of the Hongge intrusion.

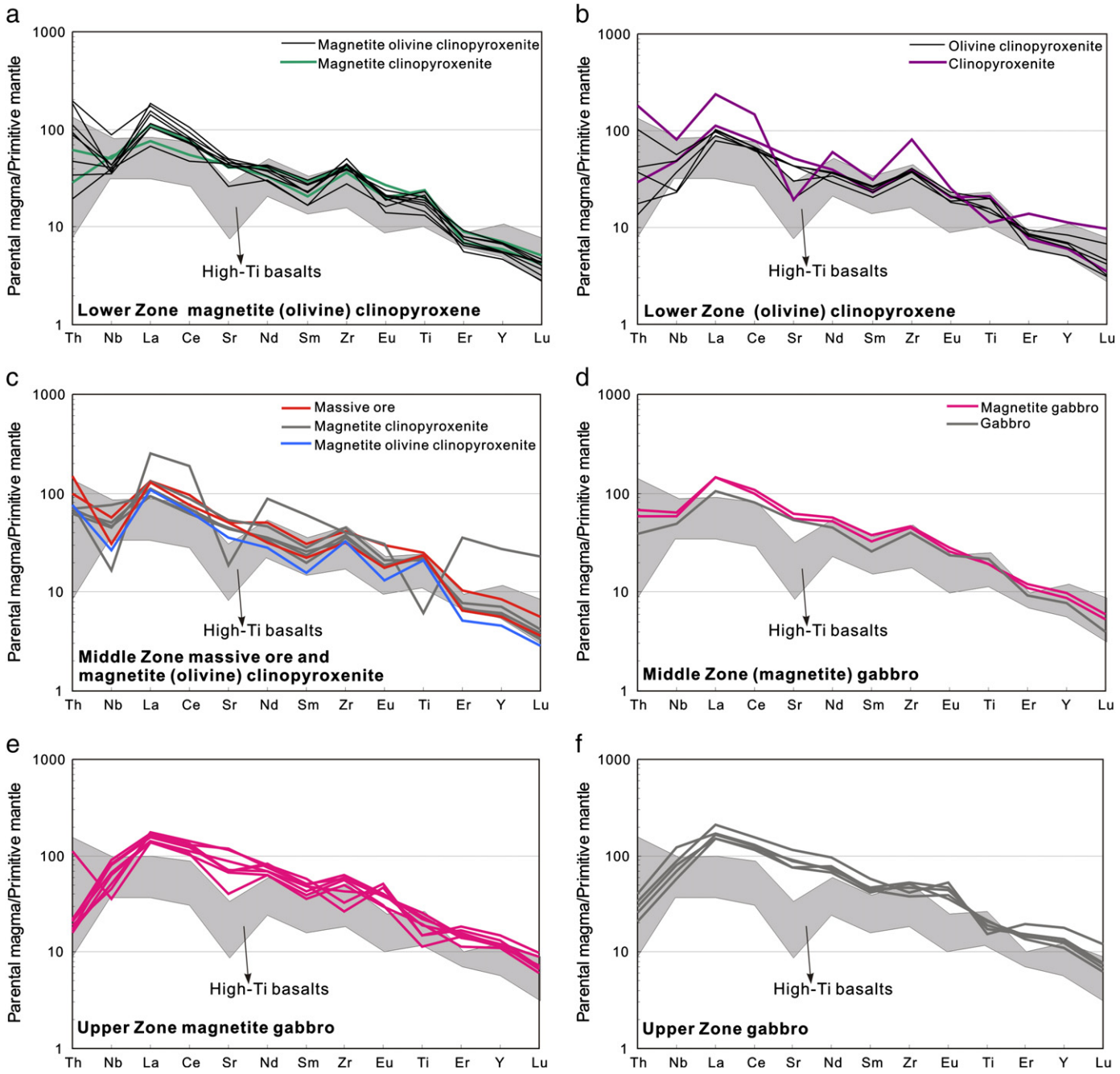

Fig. 10. Primitive-mantle normalized trace element diagrams of the parental magma in equilibrium with the clinopyroxene of the Hongge intrusion. The clinopyroxene/basaltic liquid partition coefficients used in the calculation of trace element concentrations of the parental magma are listed in Supplementary Table A4 (Rollinson, 1993; Bedard, 1994; Hauri et al., 1994; Green et al., 2000). The values for the Emeishan high-Ti basalts are from Xu et al. (2001), Xiao et al. (2004), and Song et al. (2008a). Normalization values are from Sun and McDonough (1989).

occurrence of amount of euhedral apatite in the UZ apatite (magnetite) gabbros indicates that they are solidified from a P_2O_5-saturated residual magma after the formation of the LZ and MZ in the Hongge intrusion. If the amount of new replenished magma is not too much, the mixed magma should be still P_2O_5-saturated. The lowest Th contents in parental magma in equilibrium with clinopyroxene of the UZ can be attributed to crystallization of apatite together with clinopyroxene (Fig. 10e, f), because Th is much more compatible to apatite than clinopyroxene ($D_{Th}^{Ap/Liquid} = 0.33$, Prowatke and Klemme, 2006; $D_{Th}^{Cpx/Liquid} = 0.03$, Rollinson, 1993). Thus, apatite accumulated along with silicates and Fe–Ti oxides to form the thick apatite magnetite gabbro layer in cycle IX of the UZ. Similarly, the apatite-oxide-rich rocks also occur in the upper part of the Skaergaard intrusion and the Sept-Iles intrusion (Cimon, 1998; Higgins, 2005; McBirney, 1996; Tollari et al., 2008).

7. Conclusions

(1) Although the Lower Zone of the Hongge intrusion has relatively more primitive parental magma, the introduction of external H_2O during assimilation of the footwall meta-sandstone resulted in early crystallization of magnetite. However, the amount of early crystallized magnetite is not enough to form massive oxide ore layers.

(2) The parental magma of the Middle Zone is highly Fe–Ti enriched because of extensive fractional crystallization of olivine and

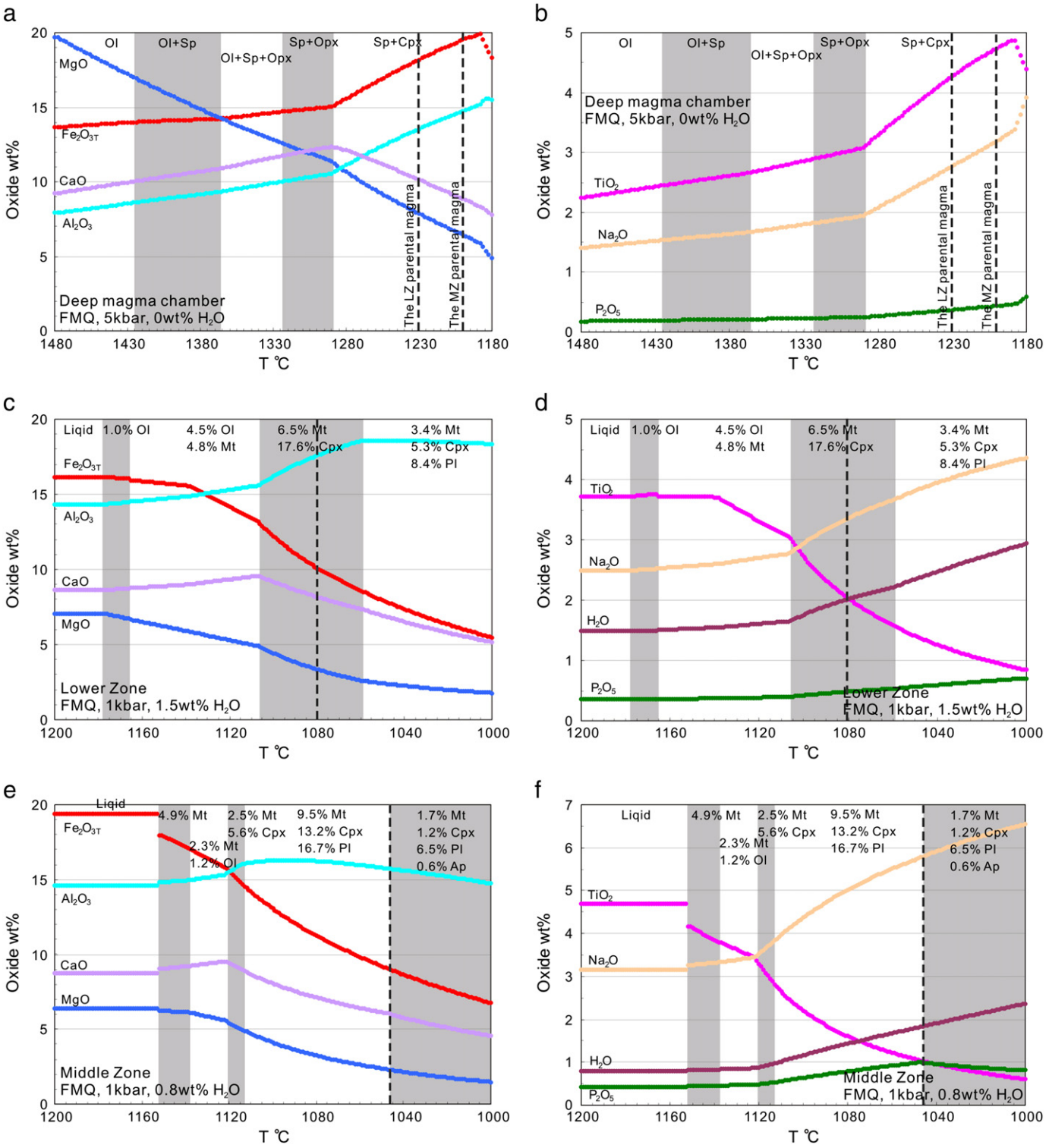

Fig. 11. a and b: MELTS modeling of fractionation of dry magma in the deep-seated magma chamber under FMQ, 5 kbar; c and d: fractionation of the parental magma of the Lower Zone of the Hongge intrusion under FMQ, 1 kbar and 1.5 wt.% H_2O; e and f: fractionation of the Middle Zone of the Hongge intrusion under FMQ, 1 kbar and 0.8 wt.% H_2O.

pyroxenes in deep-seated magma chamber. The massive oxide ore layers at the bases of each cyclic unit were produced by coupling of early and extensive crystallization of magnetite and gravitational resorting and settling of the magnetite during the magma flowing.

(3) The residual magma became saturated in P_2O_5 because of extensively fractionation during the formation of the Lower and Middle Zones. Therefore, apatite crystallized together with the silicates and Fe–Ti oxides to form the apatite magnetite gabbros in the Upper Zone.

Supplementary data to this article can be found online at http://dx.doi.org/10.1016/j.oregeorev.2013.08.010.

Acknowledgments

The authors acknowledge the constructive reviews by Kwan-Nang Pang and two anonymous referees and the editorial handling by Zhao-Chong Zhang. We also would like to thank Zhou Guo-Fu, Liu Shi-Rong and Li Liang for their efforts in electron microprobe and LA-ICP-MS analysis. This work was funded by the National Basic Research Program of China (2012CB416804) and research fund of the State Key Laboratory of Ore Deposit Geochemistry (SKLOG-ZY125-06) and NSFC research grants (40730420) to Xie-Yan Song.

References

Bai, Z.J., Zhong, H., Naldrett, A.J., Zhu, W.G., Xu, G.W., 2012. Whole-rock and mineral composition constraints on the genesis of the giant Hongge Fe–Ti–V oxide deposit in the Emeishan Large Igneous Province, Southwest China. Econ. Geol. 107, 507–524.

Baker, L.L., Rutherford, M.J., 1996. The effect of dissolved water on the oxidation state of silicic melts. Geochim. Cosmochim. Acta 60, 2179–2187.

Bedard, J.H., 1994. A procedure for calculating the equilibrium distribution of trace elements among the minerals of cumulate rocks, and the concentration of trace elements in the coexisting liquids. Chem. Geol. 118, 143–153.

Berndt, J., Liebske, C., Holtz, F., Freise, M., Nowak, M., Ziegenbein, D., Hurkuck, W., Koepke, J., 2002. A combined rapid-quench and H_2-membrane setup for internally heated pressure vessels: description and application for water solubility in basaltic melts. Am. Mineral. 87, 1717–1726.

Berndt, J., Koepke, J., Holtz, F., 2005. An experimental investigation of the influence of water and oxygen fugacity on differentiation of MORB at 200 MPa. J. Petrol. 46, 135–167.

Bindeman, I.N., Davis, A.M., Drake, M.J., 1998. Ion microprobe study of plagioclase-basalt partition experiments at natural concentration levels of trace elements. Geochim. Cosmochim. Acta. 62, 1175–1193.

Botcharnikov, R.F., Freise, M., Holtz, F., Behrens, H., 2005. Solubility of C–O–H mixtures in natural melts: new experimental data and application range of recent models. Ann. Geophys. 48, 633–646.

Botcharnikov, R.E., Almeev, R.R., Koepke, J., Holtz, F., 2008. Phase relations and liquid lines of descent in hydrous ferrobasalt — implications for the Skaergaard intrusion and Columbia River flood basalts. J. Petrol. 49, 1687–1727.

Chen, J.F., Jahn, B.M., 1998. Crustal evolution of southeastern China: Nd and Sr isotopic evidence. Tectonophysics 284, 101–133.

Chung, S.L., Jahn, B.M., 1995. Plume–lithosphere interaction in generation of the Emeishan flood basalts at the Permian–Triassic boundary. Geology 23, 889–892.

Cimon, J., 1998. L'unité à apatite de rivière des Rapides, Complexe de Sept-Îles: Localisation stratigraphique et facteurs à l'origine de sa formation. 97. Ministère des Ressources naturelles, Québec 1–32.

Dixon, J.E., Stolper, E.M., Holloway, J.R., 1995. An experimental study of water and carbon dioxide solubilities in mid ocean ridge basaltic liquids. Part I: calibration and solubility models. J. Petrol. 36, 1607–1631.

Driouch, Y., Béziat, D., Grégoire, M., Laguenini, F., Abbou, M.B., Ntarmouchant, A., Roddaz, M., Dahire, M., Bennouna, A., Belkasmi, M., Brusset, S., Debat, P., 2010. Clinopyroxene trace element compositions of cumulate mafic rocks and basalts from the Hercynian Moroccan Central Meseta: petrogenetic implications. J. Afr. Earth Sci. 56, 97–106.

Eales, H.V., Cawthorn, R.G., 1996. The Bushveld Complex. In: Cawthorn, R.G. (Ed.), Layered Intrusions. Elsevier Science, Amsterdam, pp. 181–229.

Feig, S.T., Koepke, J., Snow, J.E., 2006. Effect of water on tholeiitic basalt phase equilibria: an experimental study under oxidizing conditions. Contrib. Mineral. Petrol. 152, 611–638.

Feig, S.T., Koepke, J., Snow, J.E., 2010. Effect of oxygen fugacity and water on phase equilibria of a hygrous tholeiitic basalt. Contrib. Mineral. Petrol. 160, 551–568.

Foden, J.D., Green, D.H., 1992. Possible role of amphibole in the origin of andesite: some experimental and natural evidence. Contrib. Mineral. Petrol. 109, 479–493.

Frost, B.R., 1991. Magnetic petrology; factors that control the occurrence of magnetite in crustal rocks. Rev. Mineral. Geochem. 25, 489–509.

Frost, B.R., Lindsley, D.H., Andersen, D.J., 1988. Fe–Ti oxide-silicate equilibrium: assemblages with fayalitic olivine. Am. Mineral. 73, 727–740.

Gaetani, G.A., Grove, T.L., Bryan, W.B., 1993. The influence of water on the petrogenesis of subduction-related igneous rocks. Nature 365, 332–334.

Gaillard, F., Scaillet, B., Pichavant, M., Beny, J.M., 2001. The effect of water and f_{O2} on the ferric-ferrous ratio of silicic melts. Chem. Geol. 174, 255–273.

Ganino, C., Arndt, N.T., Zhou, M.F., Gaillard, F., Chauvel, C., 2008. Interaction of magma with sedimentary wall rock and magnetite ore genesis in the Panzhihua mafic intrusion, SW China. Miner. Deposita 43, 677–694.

Ghiorso, M.S., Sack, R.O., 1995. Chemical mass transfer in magmatic processes IV. A revised and internally consistent thermodynamic model for the interpolation and extrapolation of liquid–solid equilibria in magmatic systems at elevated temperatures and pressures. Contrib. Mineral. Petrol. 119, 197–212.

Green, T.R., Pearson, N.F., 1987. An experimental study of Nb and Ta partitioning between Ti-rich minerals and silicate liquids at high pressure and temperature. Geochim. Cosmochim. Acta 51, 55–62.

Green, T.H., Blundy, J.D., Adam, J., Yaxley, G.M., 2000. SIMS determination of trace element partition coefficients between garnet, clinopyroxene and hydrous basaltic liquids at 2–7.5 GPa and 1080–1200 °C. Lithos 53, 165–187.

Guo, F., Fan, W.M., Wang, Y.J., Li, C.W., 2004. When did the Emeishan mantle plume activity start? Geochronological and geochemical evidence from ultramafic–mafic dikes in southwestern China. Int. Geol. Rev. 46, 226–234.

Hauri, E.H., Wagner, T.P., Grove, T.L., 1994. Experimental and natural partitioning of Th, U, Pb and other trace elements between garnet, clinopyroxene and basaltic melts. Chem. Geol. 117, 149–166.

Higgins, M.D., 2005. A new interpretation of the structure of the Sept Iles Intrusive suite, Canada. Lithos 83, 199–213.

Howarth, G.H., Prevec, S.A., 2013. Hydration vs. oxidation: modelling implications for Fe–Ti oxide crystallisation in mafic intrusions, with specific reference to the Panzhihua intrusion, SW China. Geosci. Front 4, 555–569.

Howarth, G.H., Prevec, S.A., Zhou, M.F., 2013. Timing of Ti-magnetite crystallisation and silicate disequilibrium in the Panzhihua mafic layered intrusion: implications for ore-forming processes. Lithos 170–171, 73–89.

Irvine, T.N., 1977. Origin of chromitite layers in the Muskox intrusion and other stratiform intrusions: a new interpretation. Geology 5, 273–277.

Jones, J.H., 1995. Experimental trace element partitioning. In: Ahrens, T.J. (Ed.), Rock Physics & Phase Relations: A Handbook of Physical Constants. American Geophysical Union, pp. 73–104.

Jugo, P.J., Luth, R.W., Richards, J.P., 2005. An experimental study of the sulfur content in basaltic melts saturated with immiscible sulfide or sulfate liquids at 1300 °C and 1.0 GPa. J. Petrol. 46, 783–798.

Jurewicz, A.J.G., Watson, E.B., 1988. Cations in olivine, Part 1: calcium partitioning and calcium–magnesium distribution between olivines and coexisting melts, with petrologic applications. Contrib. Mineral. Petrol. 99, 176–185.

Kamenetsky, V.S., Chung, S.L., Kamenetsky, M.B., Kuzmin, D.V., 2012. Picrites from the Emeishan Large Igneous Province, SW China: a compositional continuum in primitive magmas and their respective mantle sources. J. Petrol. 53, 2095–2113.

Lee, C.A., 1996. A review of mineralization in the Bushveld Complex and some other layered intrusions. In: Cawthorn, R.G. (Ed.), Layered Intrusions. Elsevier Science, Amsterdam, pp. 103–145.

Lesne, P., Scaillet, B., Pichavant, M., Iacono-Marziano, G., Beny, J.M., 2011. The H_2O solubility of alkali basaltic melts: an experimental study. Contrib. Mineral. Petrol. 162, 133–151.

Libourel, G., 1999. Systematics of calcium partitioning between olivine and silicate melt: implications for melt structure and calcium content of magmatic olivines. Contrib. Mineral. Petrol. 136, 63–80.

Liu, Y.S., Hu, Z.C., Gao, S., Günther, D., Xu, J., Gao, C.G., Chen, H.H., 2008. In situ analysis of major and trace elements of anhydrous minerals by LA-ICP-MS without applying an internal standard. Chem. Geol. 257, 34–43.

McBirney, A.R., 1996. The Skaergaard intrusion. In: Cawthorn, R.G. (Ed.), Layered Intrusions. Elsevier Science, Amsterdam, pp. 147–180.

Mei, H.J., Xu, Y.G., Xu, J.F., Huang, X.L., He, D.C., 2003. Late Permian basalt–phonolite suite from Longzhoushan in the Panxi rift zone. Acta Geol. Sin. 77, 341–358 (in Chinese).

Namur, O., Charlier, B., Toplis, M.J., Higgins, M.D., Liégeois, J.P., Vander Auwera, J.V., 2010. Crystallization sequence and magma chamber processes in the ferrobasaltic Sept Iles layered intrusion, Canada. J. Petrol. 51, 1203–1236.

Pang, K.N., Zhou, M.F., Lindsley, D., Zhao, D.G., Malpas, J., 2008. Origin of Fe–Ti oxide ores in mafic intrusions: evidence from the Panzhihua intrusion, SW China. J. Petrol. 49, 295–313.

Pang, K.N., Li, S., Zhou, M.F., Ripley, E.M., 2009. Mineral compositional constraints on petrogenesis and oxide ore genesis of the late Permian Panzhihua layered gabbroic intrusion, SW China. Lithos 110, 199–214.

Panxi Geological Unit, 1984. Mineralization and Exploration Forecasting of V–Ti Magnetite Deposits in the Panzhihua–Xichang Region (in Chinese).

Prowatke, S., Klemme, S., 2006. Trace element partitioning between apatite and silicate melts. Geochim. Cosmochim. Acta 70, 4513–4527.

Qi, L., Wang, C.Y., Zhou, M.F., 2008. Controls on the PGE distribution of Permian Emeishan alkaline and peralkaline volcanic rocks in Longzhoushan, Sichuan Province, SW China. Lithos 106, 222–236.

Rollinson, H.R., 1993. Using Geochemical Data: Evaluation, Presentation, Interpretation. Longman Scientific & Technical, New York.

She, Y.-W., Yu, S.-Y., Song, X.-Y., Chen, L.-M., Zheng, W.-Q., Luan, Y., 2014. The formation of P-rich Fe -Ti oxide ore layers in the Taihe layered intrusion, SW China: implications for magma-plumbing system process. Ore Geol. Rev. 57, 539–559.

Scoon, R.N., Mitchell, A.A., 1994. Discordant iron-rich ultramafic pegmatites in the Bushveld Complex and their relationship to iron-rich intercumulus and residual liquids. J. Petrol. 35, 881–917.

Sobolev, A.V., Chaussidon, M., 1996. H_2O concentrations in primary melts from supra-subduction zones and mid-ocean ridges: implications for H_2O storage and recycling in the mantle. Earth Planet. Sci. Lett. 137, 45–55.

Sobolev, A.V., Krivolutskaya, N.A., Kuzmin, D.V., 2009. Petrology of the parental melts and mantle sources of Siberian trap magmatism. Petrology 17, 253–286.

Song, X.Y., Zhou, M.F., Hou, Z.Q., Cao, Z.M., Wang, Y.L., Li, Y.G., 2001. Geochemical constraints on the mantle source of the upper Permian Emeishan continental flood basalts, southwestern China. Int. Geol. Rev. 43, 213–225.

Song, X.Y., Zhou, M.F., Cao, Z.M., Robinson, P.T., 2004. Late Permian rifting of the South China Craton caused by the Emeishan mantle plume? J. Geol. Soc. London 161, 773–781.

Song, X.Y., Zhang, C.J., Hu, R.Z., Zhong, H., Zhou, M.F., Ma, R.Z., Li, Y.G., 2005. Genetic links of magmatic deposits in the Emeishan large igneous province with dynamics of mantle plume. J. Mineral. Petrol. 25, 33–44 (in Chinese).

Song, X.Y., Qi, H.W., Robinson, P.T., Zhou, M.F., Cao, Z.M., Chen, L.M., 2008a. Melting of the subcontinental lithospheric mantle by the Emeishan mantle plume; evidence from the basal alkaline basalts in Dongchuan, Yunnan, Southwestern China. Lithos 100, 93–111.

Song, X.Y., Zhou, M.F., Tao, Y., Xiao, J.F., 2008b. Controls on the metal compositions of magmatic sulfide deposits in the Emeishan large igneous province, SW China. Chem. Geol. 253, 38–49.
Song, X.Y., Keays, R.R., Xiao, L., Qi, H.W., Ihlenfeld, C., 2009. Platinum-group element geochemistry of the continental flood basalts in the central Emeisihan Large Igneous Province, SW China. Chem. Geol. 262, 246–261.
Song, X.Y., Qi, H.W., Hu, R.Z., Chen, L.M., Yu, S.Y., Zhang, J.F., 2013. Formation of thick stratiform Fe–Ti oxide layers in layered intrusion and frequent replenishment of fractionated mafic magma: evidence from the Panzhihua intrusion, SW China. Geochem. Geophys. Geosyst. 14, 712–732.
Stone, W.E., Deloule, E., Larson, M.S., Lesher, C.M., 1997. Evidence for hydrous high-MgO melts in the Precambrian. Geology 25, 143–146.
Sun, S.S., McDonough, W.F., 1989. Chemical and isotopic systematics of oceanic basalts: implications for mantle composition and processes. In: Saunders, A.D., Norry, M.J. (Eds.), Magmatism in the Ocean Basin. Geol. Soc. Lond. Spec. Publ., 42, pp. 313–345.
Tao, Y., Ma, Y.S., Miao, L.C., Zhu, F.L., 2009. SHRIMP U–Pb zircon age of the Jinbaoshan ultramafic intrusion, Yunnan Province, SW China. Chin. Sci. Bull. 54, 168–172.
Tollari, N., Baker, D.R., Barnes, S.J., 2008. Experimental effects of pressure and fluorine on apatite saturation in mafic magmas, with reference to layered intrusions and massif anorthosites. Contrib. Mineral. Petrol. 156, 161–175.
Wang, C.Y., Zhou, M.F., Qi, L., 2007. Permian flood basalts and mafic intrusions in the Jinping (SW China)-Song Da (northern Vietnam) district: mantle sources, crustal contamination and sulfide segregation. Chem. Geol. 243, 317–343.
Xiao, L., Xu, Y.G., He, B., 2003. Emei mantle plume–subcontinental lithosphere interaction: Sr–Nd and O isotopic evidences from low-Ti and high-Ti basalts. Geol. J. China Univ. 9, 207–217 (in Chinese).
Xiao, L., Xu, Y.G., Mei, H.J., Zheng, Y.F., He, B., Pirajno, F., 2004. Distinct mantle sources of low-Ti and high-Ti basalts from the western Emeishan large igneous province, SW China: implications for plume–lithosphere interaction. Earth Planet. Sci. Lett. 228, 525–546.
Xu, Y.G., Chung, S.L., Jahn, B.M., Wu, G.Y., 2001. Petrologic and geochemical constraints on the petrogenesis of Permian–Triassic Emeishan flood basalts in southwestern China. Lithos 58, 145–168.
Xu, Y.G., Luo, Z.Y., Huang, X.L., He, B., Xiao, L., Xie, L.W., Shi, Y.R., 2008. Zircon U–Pb and Hf isotope constraints on crustal melting associated with the Emeishan mantle plume. Geochim. Cosmochim. Acta 72, 3084–3104.
Yu, S.-Y., Song, X.-Y., Chen, L.-M., Li, X.-B., 2014. Postdated melting of subcontinental lithospheric mantle by the Emeishan mantle plume: evidence from the Anyi intrusion, Yunnan, SW China. Ore Geol. Rev. 57, 560–573.
Zhang, Z.C., Mao, J.W., Saunders, A.D., Ai, Y., Li, Y., Zhao, L., 2009. Petrogenetic modeling of three mafic–ultramafic layered intrusions in the Emeishan large igneous province, SW China, based on isotopic and bulk chemical constraints. Lithos 113, 369–392.
Zhang, X.Q., Song, X.Y., Chen, L.M., Xie, W., Yu, S.Y., Zheng, W.Q., Deng, Y.F., Zhang, J.F., Gui, S.G., 2012. Fractional crystallization and the formation of thick Fe–Ti–V oxide layers in the Baima layered intrusion, SW China. Ore Geol. Rev. 49, 96–108.
Zhong, H., Zhu, W.G., 2006. Geochronology of layered mafic intrusions from the Pan-Xi area in the Emeishan large igneous province, SW China. Miner. Deposita 41, 599–606.
Zhou, M.F., Malpas, J., Song, X.Y., Robinson, P.T., Sun, M., Kennedy, A.K., Lesher, C.M., Keays, R.R., 2002. A temporal link between the Emeishan large igneous province (SW China) and the end-Guadalupian mass extinction. Earth Planet. Sci. Lett. 196, 113–122.
Zhou, M.F., Robinson, P.T., Lesher, C.M., Keays, R.R., Zhang, C.J., Malpas, J., 2005. Geochemistry, petrogenesis and metallogenesis of the Panzhihua gabbroic layered intrusion and associated Fe–Ti–V oxide deposits, Sichuan Province, SW China. J. Petrol. 46, 2253–2280.
Zhou, M.F., Zhao, J.H., Qi, L., Su, W.C., Hu, R.Z., 2006. Zircon U–Pb geochronology and elemental and Sr–Nd isotope geochemistry of Permian mafic rocks in the Funing area, SW China. Contrib. Mineral. Petrol. 151, 1–19.
Zhou, M.F., Arndt, N.T., Malpas, J., Wang, C.Y., Kennedy, A.K., 2008. Two magma series and associated ore deposit types in the Permian Emeishan large igneous province, SW China. Lithos 103, 352–368.
Zindler, A., Hart, S., 1986. Chemical geodynamics. Annu. Rev. Earth Planet. Sci. 14, 493–571.